Generation of high-dimensional qudit quantum states via two-dimensional quantum walks

Chiara Esposito,[1] Francesco Di Colandrea ⬤,[2] Francesco Hoch,[1] Gonzalo Carvacho ⬤,[1] Filippo Cardano,[2]
Nicolò Spagnolo ⬤,[1] Lorenzo Marrucci,[2] and Fabio Sciarrino ⬤[1,*]

[1]*Dipartimento di Fisica, Sapienza Università di Roma, Piazzale Aldo Moro 5, I-00185 Roma, Italy*
[2]*Dipartimento di Fisica "Ettore Pancini," Università degli Studi di Napoli Federico II,*
Complesso Universitario di Monte Sant'Angelo, via Cintia, 80126 Napoli, Italy

Several quantum protocols, with applications ranging from fundamental studies to cryptographic scenarios, can be enhanced through the generation and manipulation of quantum states that belong to high-dimensional Hilbert spaces. For this reason, it is worth devoting efforts to find more efficient methods for complex qudit-state generation. One-dimensional quantum walks have proved to be efficient and versatile platforms for the engineering of such complex states. Hitherto, however, using their two-dimensional counterpart for this task has remained unexplored. In this paper, we consider two-dimensional quantum walk evolution as a tool for the generation of high-dimensional qudit states. We theoretically prove that a suitable change of the coin operators at each step permits the generation of a subset of qudit states by using less resources with respect to the one-dimensional counterpart. Then, we successfully generate qudit states by exploiting two-dimensional quantum walks on an experimental photonic platform. The walker position is encoded on discrete sets of optical modes carrying quantized amounts of transverse momentum and the mode couplings are actively controlled via liquid-crystal devices. The obtained results provide insight into qudit generation for applications in quantum communication and quantum cryptography.

I. INTRODUCTION

High-dimensional quantum systems, described by qudit states, are implemented on several quantum information protocols for quantum computation [1–3] and quantum sensing [4]. In comparison with the qubit case, qudit-state implementations lead to higher security and transmission rates in quantum communication [5–7] and quantum cryptography [8–10] as well as the extension of fundamental studies due to their naturally richer entanglement structure [11–13]. Qudits have been experimentally realized with different platforms such as superconductive cavities [3,14,15], ion systems [16–18], and photonic setups [13,19–21]. Photons represent suitable information carriers to encode and manipulate qudits by exploiting several degrees of freedom such as polarization [22,23], paths [24], orbital angular momentum [20,21], temporal modes, and frequency [25–27].

Quantum walks (QWs) [28] have been introduced to model either the discrete time or continuous time dynamics of a "walker," that is, a quantum particle, on a discrete lattice. Within this paper, we will exclusively refer to the discrete time case. The movements of the walker at each time step depend on the state of its internal degree of freedom, i.e., the "coin." This simple model finds several applications in quantum information and computation fields, such as quantum search algorithms [29], quantum gates for universal quantum computation [30–33], and quantum simulations [34–41]. Moreover, QW dynamics enable the generation of complex qudit states [20,24,42–49]. The output of a QW evolution can be described as a hybrid-entangled state between walker position and coin degrees of freedom [24,43–45,47–49]. This kind of entanglement involves different degrees of freedom of the same particle, i.e., it is an intrasystem entanglement [50–53], representing a resource for quantum information and quantum communication processing [54–56]. One-dimensional quantum walks (1DQWs) allow manipulating simultaneously several characteristics of qudit quantum systems [20,46–49]. Two-dimensional quantum walks (2DQWs) have been only recently exploited for improved performances in different quantum applications [57–59]. However, their capabilities of efficiently generating quantum states are currently a less explored direction.

The 1DQW is a universal tool for qudit generation, i.e., it enables the generation of a generic qudit state [20,60]. The aim of the present paper is to investigate the generation of single-particle qudit quantum states by exploiting a 2DQW evolution. From a theoretical perspective, we investigate the constraints involved in the generation of qudit states from a 2DQW with a step-dependent coin. We show that the quadratic increase of the output-state dimensionality with the step number in the 2DQW implies that universal state generation cannot be achieved, regardless of the experimental

---

implementation. On the other hand, when targeting the generation of qudit states with a fixed dimension d, we show that 2DQWs can be devised so as to require less resources with respect to the 1D counterpart.

For qudit state generation via QWs, we exploit a photonic 2DQW based on g plates [41], i.e., tunable liquid-crystal devices able to add or subtract a fixed amount of transverse momentum to photons, depending on their polarization state being left or right circular, respectively. These devices have recently been exploited for the simulation of quantum topology [41,61], multiparticle QW evolutions [62], and Bloch oscillation effects [63], and have been recently generalized to more sophisticated devices enabling the simulation of ultra-long QWs [64]. In the next sections, we address the theoretical background of the 2D split-step quantum walk (2DssQW) we use in our experimental demonstration. Then, we focus on the amplitude probability constraints of an output state when evolving within 2DQWs. From the experimental side, we generate a set of states in both classical and quantum regimes, showing the capability of reaching high-fidelity values with respect to target states.

II. THEORETICAL BACKGROUND

Here, we discuss the generation of qudit states via 2DssQWs. By considering a square lattice, a walker is described by a state $|\psi\rangle \in \mathcal{H} = \mathcal{H}_x \otimes \mathcal{H}_y \otimes \mathcal{H}_c$. If the coin is a two-level internal degree of freedom, the walker state is generally given by

$$|\psi\rangle = \sum_{i,j=-\infty}^{\infty} c_{i,j,\uparrow}|i, j, \uparrow\rangle + c_{i,j,\downarrow}|i, j, \downarrow\rangle, \qquad (1)$$

where the indices (i, j) label the position on the lattice, and $|i, j\rangle$ are the basis vectors of the Hilbert space $\mathcal{H}_{x,y} = \mathcal{H}_x \otimes \mathcal{H}_y$. The internal space $\mathcal{H}_c$ is spanned by the basis states $\{|\uparrow\rangle, |\downarrow\rangle\}$.

Starting from an initial state $|\psi_0\rangle$, the state of the system evolves under the action of a unitary operator $\tilde{U}$ at each step. In 1DQWs the operator $\tilde{U}$ can be realized as the product of a coin rotation C and a coin-dependent translation $\tilde{T}$:

$$\tilde{U} = \tilde{T}C(\theta, \xi, \zeta) \qquad (2)$$

with

$$\tilde{T} = \sum_{i=-\infty}^{+\infty} |i - 1, \uparrow\rangle\langle i, \downarrow| + |i + 1, \downarrow\rangle\langle i, \uparrow|. \qquad (3)$$

The coin operator is defined in terms of three phase parameters $\theta, \xi,$ and ζ as

$$C(\theta, \xi, \zeta) = \mathbb{I}_{x,y} \otimes \begin{pmatrix} e^{i\xi}\cos\theta & e^{i\zeta}\sin\theta \\ -e^{-i\zeta}\sin\theta & e^{i\xi}\cos\theta \end{pmatrix}. \qquad (4)$$

In order to simplify the treatment, we can now exploit the fact that, when starting from a single site and depending on the number of steps, the operator $\tilde{T}$ will populate only odd or even displaced sites. In particular, the leftmost populated site on the lattice is obtained by translating by -1 at each step. Assuming, without loss of generality, that the initial localized walker state is located in $i = 0$, these two features allow one

to remap the process in the following equivalent way:

$$T = \sum_{i=0}^{+\infty} |i, \uparrow\rangle\langle i, \downarrow| + |i + 1, \downarrow\rangle\langle i, \uparrow|, \qquad (5)$$

in which the negative displacements are replaced by a stationary step, so as to keep fixed the leftmost populated lattice site and to compress by a factor 2 the spatial evolution dynamics at all times. Notice that this is a one-to-one mapping, hence all the considerations that can be made for the quantum walk with single step operators $U = TC(\theta, \xi, \zeta)$ can be extended to $\tilde{U}$ and vice versa. In the 2DssQW the evolution at each step is divided in two split-step evolutions which correspond to the independent action of operators $U_x = T_x C_x$ and $U_y = T_y C_y$ along the x and y direction on the lattice, respectively. T_x and T_y have the same form of operator T in Eq. (5) acting on $\mathcal{H}_x \otimes \mathcal{H}_c$ and $\mathcal{H}_y \otimes \mathcal{H}_c$, respectively. The operators C_x and C_y are given by $C_x = C(\theta_x, \xi_x, \zeta_x)$ and $C_y = C(\theta_y, \xi_y, \zeta_y)$, where the generic coin operator C is defined in Eq. (4). The composed actions of these operators correspond to a single-step evolution operator $U = U_y U_x$. The actions of the split-step operators are given by

$$|\varphi_n\rangle = U_x(U^{n-1}|\psi_0\rangle), \quad |\psi_n\rangle = U^n|\psi_0\rangle, \qquad (6)$$

where n is the index of the step, and $|\varphi_n\rangle$ and $|\psi_n\rangle$ are the states obtained by evolving the initial state $|\psi_0\rangle$ under the action of odd and even split-step operators, respectively. They can be written as

$$|\varphi_n\rangle = \sum_{i,j} l_{i,j,\uparrow}^{(n)}|i, j, \uparrow\rangle + l_{i,j,\downarrow}^{(n)}|i, j, \downarrow\rangle, \qquad (7)$$

$$|\psi_n\rangle = \sum_{i,j} u_{i,j,\uparrow}^{(n)}|i, j, \uparrow\rangle + u_{i,j,\downarrow}^{(n)}|i, j, \downarrow\rangle, \qquad (8)$$

where $l_{i,j,\sigma}^{(n)}$ and $u_{i,j,\sigma}^{(n)}$ are defined as the amplitude coefficients of the state after odd or even split-step evolution. At each step, the single-step operator depends on all the coin parameters that continuously change through the entire evolution. For this reason, the evolution of the initial state at the Nth step is given by

$$|\psi_N(w)\rangle = \prod_{i=1}^{N}(T_y C_{y,i} T_x C_{x,i})|\psi_0\rangle, \qquad (9)$$

where the operators $C_{x,i} = C(\theta_{x,i}, \xi_{x,i}, \zeta_{x,i})$ and $C_{y,i} = C(\theta_{y,i}, \xi_{y,i}, \zeta_{y,i})$ are arbitrary coin operators at each step. Hence, the entire evolution is characterized by the set of coin parameters given by $w = \{\theta_{y,i}, \xi_{y,i}, \zeta_{y,i}, \theta_{x,i}, \xi_{x,i}, \zeta_{x,i}\}_{i=1}^{N}$. An alternative way to describe the final state of the 2DssQW is given by the vectors $\vec{l}_{i,j}^{\,(n)}$ and $\vec{u}_{i,j}^{\,(n)}$ for odd and even split-step evolutions. These vectors regroup the complex amplitudes of the modes at the Nth step that are generated by the same mode (i, j) at the previous split-step evolution. These vectors are defined respectively as [60]

$$\vec{l}_{i,j}^{\,(n)} = \begin{pmatrix} l_{i,j,\uparrow}^{(n)} \\ l_{i+1,j,\downarrow}^{(n)} \end{pmatrix} = C_{x,n} \begin{pmatrix} u_{i,j,\uparrow}^{(n-1)} \\ u_{i,j,\downarrow}^{(n-1)} \end{pmatrix}, \qquad (10)$$

$$\vec{u}_{i,j}^{\,(n)} = \begin{pmatrix} u_{i,j,\uparrow}^{(n)} \\ u_{i,j+1,\downarrow}^{(n)} \end{pmatrix} = C_{y,n} \begin{pmatrix} l_{i,j,\uparrow}^{(n)} \\ l_{i,j,\downarrow}^{(n)} \end{pmatrix}. \qquad (11)$$
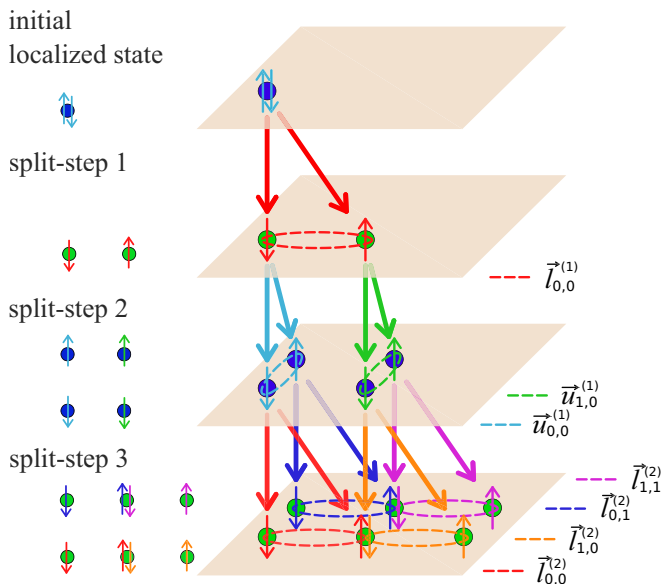
FIG. 1. Definition of the vectors $\vec{l}_{i,j}^{\,(n)}$ and $\vec{u}_{i,j}^{\,(n)}$ for the initial three split-step evolution. In order to highlight the components of the vectors $\vec{l}_{i,j}^{\,(n)}$ and $\vec{u}_{i,j}^{\,(n)}$ for each split step, we show the initial three split-step evolution on different planes. The up and down arrows represent the coin state of each site. The dashed circles regroup the components of the vectors $\vec{l}_{i,j}^{\,(n)}$ for odd split steps and $\vec{u}_{i,j}^{\,(n)}$ for even split steps. The different colors refer to different vectors. Finally, the arrows that connect the sites belonging to different planes show which site at the previous step originates the components of the vectors $\vec{l}_{i,j}^{\,(n)}$ and $\vec{u}_{i,j}^{\,(n)}$.

We stress here that these vectors do not represent the polarization states of the site (i, j). Indeed, they are not normalized. In this sense, Eqs. (10) and (11) have to be read as numerical relations between complex numbers. The validity of these numerical relations is guaranteed by the action of the translation operators. Indeed, starting from the site i, the action of the translation operator consists in shifting and flipping the $|\uparrow\rangle$ component to site $i + 1$ without changing the phase-amplitude relation between orthogonal coin states. Figure 1 depicts the relation between the coefficients of the QW state at each site and the vectors defined in Eqs. (10) and (11).

In the following section, we find specific constraints for a generic state $|\psi_N\rangle$ produced by QW evolutions.

III. THEORETICAL RESULTS

In this section, we illustrate a procedure for the generation of qudit states $|\phi\rangle$ through a 2DssQW evolution of a seed state $|\psi_0\rangle$ and a projection on a generic coin $|p\rangle$. This procedure for qudit generation is sketched in Fig. 2. As a first step, we provide constraints for the output states $|\psi_N\rangle$ of a 2DssQW that belong to the Hilbert space $\mathcal{H} = \mathcal{H}_x \otimes \mathcal{H}_y \otimes \mathcal{H}_c$. By projecting these states on an arbitrarily chosen coin, we obtain the set of states, denoted as $|\phi\rangle$, that live in the Hilbert space $\mathcal{H}_{xy} = \mathcal{H}_x \otimes \mathcal{H}_y$. In 1DQWs, this procedure has been demonstrated to be a universal tool for qudit generation [20,60]. Here we theoretically prove that the states that can be generated with this approach by using 2DssQW evolution do not span the whole Hilbert space $\mathcal{H}_{xy}$. Moreover, we show that the
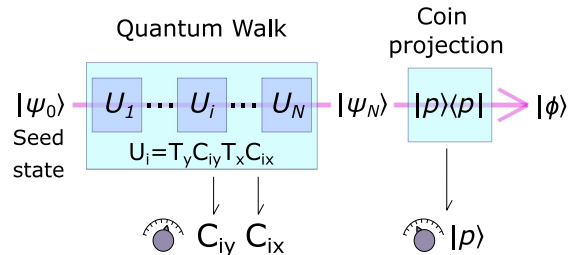

FIG. 2. Conceptual scheme of a quantum state generation via an Nth-step quantum walk evolution. The seed state $|\psi_0\rangle \in \mathcal{H}$ evolves within a 2DQW with arbitrary coin operators denoted as $C_{i,x}$ and $C_{i,y}$, where i is the step index. The operators T_x and T_y denote the translation operators along x and y directions, respectively. By changing the coin parameters at each step and by projecting on the polarization state $|p\rangle$, we can obtain the output states $|\phi\rangle \in \mathcal{H}_{xy}$.

generation of qudits by using this procedure is not universal for all 2DQW evolutions. On the other hand, it enables generating high-dimensional qudits using significantly less resources with respect to the 1D implementation. In the following, we show and discuss in detail these results.

A. Constraints on the output states

Starting from an initially localized state in the position $(0,0)$ of the lattice, with a generic coin state as *seed* state

$$|\psi_0\rangle = u_{0,0,\uparrow}^{(0)}|0, 0, \uparrow\rangle + u_{0,0,\downarrow}^{(0)}|0, 0, \downarrow\rangle, \qquad (12)$$

we derive the constraints on the amplitudes for each odd and even split step. The constraints on the amplitudes of the output state of the 2DQW at the Nth step derive from the unitarity of the single-step operator U. In particular, the translation operator along the x or y direction always splits a localized state in two orthogonally polarized states, positioned in the two adjacent sites, as shown in Fig. 1. For instance, the localized state $|\psi_0\rangle$ in the site $(0,0)$ evolves in a superposition of $|0, 0, \downarrow\rangle$ and $|1, 0, \uparrow\rangle$, by applying the translation operator T_x. By considering $|0, 0, \downarrow\rangle$ and $|1, 0, \uparrow\rangle$ as a localized initial state of the 2DQW, the corresponding evolved states $U_y C_x|0, 0, \downarrow\rangle$ and $U_y C_x|1, 0, \uparrow\rangle$ will be orthogonal, because of the unitarity of U_y and C_x. It then leads to the constraints on the amplitudes of the evolved state $|\psi_1\rangle = U|\psi_0\rangle$, reported below. The complete and detailed demonstration of the constraints for each odd and even split step is reported in Appendix A.

The general constraint rules for an odd and even split step of a 2DssQW are given in the following. Even split steps $N = 2M$ correspond to real 2DQW steps with constraints given by

$$u_{i,0,\downarrow}^{(N)} = u_{i,N,\uparrow}^{(N)} = 0, \qquad (13)$$

$$\sum_{i=0}^{N-h}\sum_{j=0}^{N-k-1} \vec{u}_{i,j}^{\,(N)\dagger} \cdot \vec{u}_{i+h,j+k}^{\,(N)} = 0 \begin{cases} h = 1, \ldots, N \\ k = 0, \ldots, N-1 \end{cases}, \qquad (14)$$

$$\sum_{i=0}^{N-h}\sum_{j=0}^{N-k-1} \vec{u}_{i,j+k}^{\,(N)\dagger} \cdot \vec{u}_{i+h,j}^{\,(N)} = 0 \begin{cases} h = 0, \ldots, N \\ k = 1, \ldots, N-1 \end{cases}. \qquad (15)$$

The conditions for the odd split steps $N = 2M + 1$ are given by

$$l_{0,i,\downarrow}^{(N)} = l_{N,i,\uparrow}^{(N)} = 0, \tag{16}$$

$$\sum_{i=0}^{N-h} \sum_{j=0}^{N-k} \vec{l}_{i,j}^{(N+1)\dagger} \cdot \vec{l}_{i+h,j+k}^{(N+1)} = 0 \begin{cases} h = 1, \ldots, N \\ k = 0, \ldots, N \end{cases}, \tag{17}$$

$$\sum_{i=0}^{N-h} \sum_{j=0}^{N-k} \vec{l}_{i,j+k}^{(N+1)\dagger} \cdot \vec{l}_{i+h,j}^{(N+1)} = 0 \begin{cases} h = 0, \ldots, N \\ k = 1, \ldots, N \end{cases}. \tag{18}$$

In Appendix A, we also show a graphical approach to obtain these conditions at the $2M$ and $2M + 1$ split steps. It is worth noticing that the number of conditions grows quadratically with the number of steps. As we explain in the following, the number of independent parameters increases linearly with the number of steps. For this reason, it is not possible to realize an arbitrary state in the 2D walker space. This constraint provides a condition on the states that can be generated using a 2DssQW platform.

B. Projection on the coin state

The output state $|\psi_N\rangle$ of the 2DssQW evolution at the Nth step can be written as

$$|\psi_N\rangle = \sum_{i=0}^{N} u_{i,0,\uparrow}^{(N)} |i, 0, \uparrow\rangle + u_{i,N,\downarrow}^{(N)} |i, N, \downarrow\rangle$$
$$+ \sum_{i=0}^{N} \sum_{j=1}^{N-1} u_{i,j,\uparrow}^{(N)} |i, j, \uparrow\rangle + u_{i,j,\downarrow}^{(N)} |i, j, \downarrow\rangle, \tag{19}$$

where the coefficients $u_{i,j,\uparrow}^{(N)}$ fulfill the constraints in Eqs. (14) and (15). In Appendix B, we report the set of coin operators necessary to generate such states $|\psi_N\rangle$. If we project the output on a generic coin, we obtain a state $|\phi\rangle$, that lives in the Hilbert space $\mathcal{H}_{xy} = \mathcal{H}_x \otimes \mathcal{H}_y$ and that can be written as

$$|\phi\rangle = \sum_{i=0}^{N} \sum_{j=0}^{N} u_{i,j} |i, j\rangle. \tag{20}$$

This state can also be seen as the projection of the state $|\psi_N\rangle$ on the coin state $|p\rangle$ given by

$$|p\rangle = \cos\frac{\theta}{2}|\uparrow\rangle + \sin\frac{\theta}{2} e^{i\varphi}|\downarrow\rangle. \tag{21}$$

In this term we can write the state $|\phi\rangle$ as

$$|\phi\rangle = \sum_{i=0}^{N} \left(\cos\frac{\theta}{2} u_{i,0,\uparrow}^{(N)} |i, 0\rangle + \sin\frac{\theta}{2} e^{-i\varphi} u_{i,N,\downarrow}^{(N)} |i, N\rangle \right)$$
$$+ \sum_{i=0}^{N} \sum_{j=1}^{N-1} \left(\cos\frac{\theta}{2} u_{i,j,\uparrow}^{(N)} + \sin\frac{\theta}{2} e^{-i\varphi} u_{i,j,\downarrow}^{(N)} \right) |i, j\rangle. \tag{22}$$

By comparing Eq. (20) with Eq. (22) we obtain the following equations:

$$u_{i,0} = \cos\frac{\theta}{2} u_{i,0,\uparrow}^{(N)}, \quad u_{i,N} = \sin\frac{\theta}{2} e^{-i\varphi} u_{i,N,\downarrow}^{(N)},$$
$$u_{i,j} = \cos\frac{\theta}{2} u_{i,j,\uparrow}^{(N)} + \sin\frac{\theta}{2} e^{-i\varphi} u_{i,j,\downarrow}^{(N)} \quad \text{with } j \neq 0, N. \tag{23}$$

Hence, the state $u_{i,j}$ can be generated if there exist $u_{i,j}^{(N)}$ (complex variables) and θ, φ (real variables) that simultaneously fulfill the constraints of Eqs. (13)–(15) and (23). It is straightforward to demonstrate that the number of independent variables is lower than the number of constraint equations at each step. Hence, we can only realize a 2D state that belongs to a subset of the complete Hilbert space $\mathcal{H}_{xy}$. The nonuniversality of the 2DQW generation is addressed in detail in the following section.

C. Nonuniversality of 2DQWs

In this section, we address the capability of 2DQWs of generating quantum states in the Hilbert space $\mathcal{H}_{xy} = \mathcal{H}_x \otimes \mathcal{H}_y$. In particular, we will prove that there is a natural limit related to the universality of the states that can be constructed through 2DQW evolutions by using an intuitive argument. In a 1DQW, the independent parameters of the coin and the state increase linearly. This condition is necessary for a universal generation of qudit states in a 1DQW, as theoretically and experimentally proved in Refs. [20,60].

The single-step operator U of a 2DssQW is composed by two arbitrary coin operators, i.e., SU(2) unitary matrices, which have three independent real-valued parameters. Then we can freely choose a coin $|p\rangle$ to project the QW output state, which adds two independent real-valued parameters. Hence, at the Nth step, we can control $6N + 2$ real-valued parameters, while the generated state belongs to a Hilbert space of dimension $(N + 1)^2$. For this reason, the independent real-valued parameters are $2(N + 1)^2 - 2$, where the two constraints are the normalization and the arbitrariness of the global phase of the state. Hence, the independent parameters related to the coin operators and projection are not enough to completely determine all the coefficients of the output state.

The same argument can be exploited for a 2DQW with coins of arbitrary dimensions and with translation invariant symmetry, i.e., that do not admit the presence of space-dependent operations. Indeed, the number of coin operators always increases linearly with the number of steps, while the dimension of the output states increases quadratically. The argument reported here is valid regardless of the experimental platform for the 2DQW implementation. For this reason, 2DQWs are not universal for qudit state generation.

On the other hand, the quadratic increase in the dimension of the Hilbert space for the output states allows one to realize a state involving a fixed number of modes by using less resources with respect to the 1D counterpart. In fact, the generation of a state with $(N + 1)^2$ modes through 1DQW evolutions requires at least $(N + 1)^2 - 1$ steps. In a 2DQW evolution, a state with $(N + 1)^2$ modes can be realized by only implementing N steps. Experimentally, a lower number of steps corresponds to requiring less devices to perform the complete evolution, thus leading to reduced losses for the generation of the same state. Finally, the 2D platform may be employed to generate intraparticle entanglement between two orthogonal walker components, as described by Eq. (20) [21].

In the following, we provide a numerical characterization for the set of states that can be generated by exploiting one, two, and three steps of 2DssQW evolutions. For this purpose, we calculate the state at the output of the two-dimensional
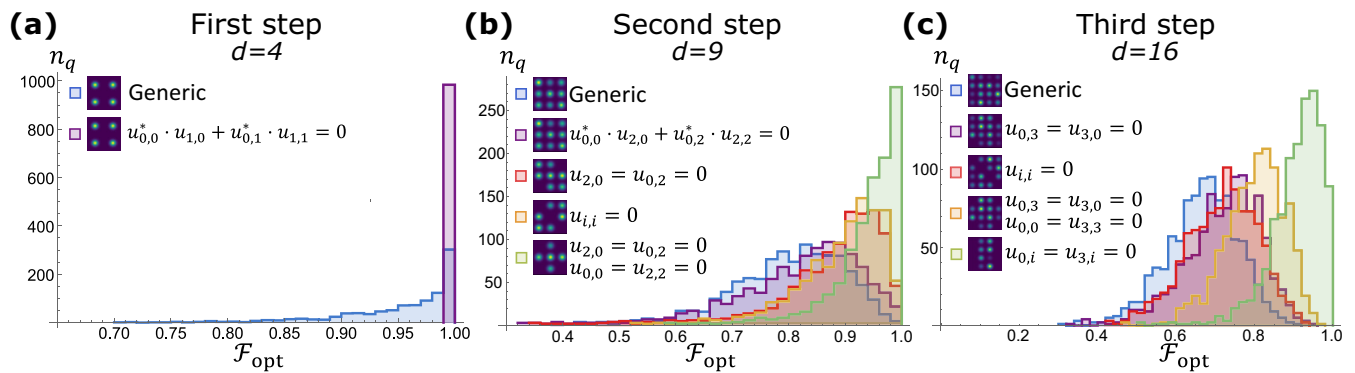
FIG. 3. Histograms of fidelity values for qudit states generated by one, two, and three steps of 2DssQW evolutions. We calculate the fidelity between 1000 randomly chosen qudit states with dimensions (a) $d = 4$, (b) $d = 9$, and (c) $d = 16$ and the states generated through 2DssQW evolution that represents the best approximation of the randomly chosen states. The fidelity values are collected. In order to verify which class of states can be better generated by 2DssQW evolution, we impose different conditions (insets) on the chosen qudit states.

quantum walk for one, two, and three steps. Then, we randomly generate qudit states with dimensions $d = 4, 9,$ and 16 for the first, second, and third step, respectively. We evaluate the fidelity $\mathcal{F} = |\langle \phi_{\text{out}} | \phi_{\text{ran}} \rangle|^2$ between the output and the randomly generated states as a function of the parameters of the quantum walk evolution and we minimize with respect to these parameters the cost function $\mathcal{G} = 1 - \mathcal{F}$. As a result of each minimization, we obtain a qudit state $|\phi_{\text{opt}}\rangle$ which maximizes the fidelity value with the randomly chosen qubit and it is achievable via a 2DssQW evolution. In order to quantify the goodness of the approximation, we calculate the fidelity $\mathcal{F}_{\text{opt}} = |\langle \phi_{\text{opt}} | \phi_{\text{ran}} \rangle|^2$ between each randomly chosen qudit state and the correspondent qudit state obtained as a result of the minimization.

In Fig. 3, we report different histograms of $\mathcal{F}_{\text{opt}}$ by imposing different conditions on randomly chosen qudit with dimension $d = 4, 9,$ and 16, respectively. In particular, we randomly extract qudits and we act on them so that they satisfy all constraints. We notice that the mean fidelity increases, by reducing the number of qudit-state independent parameters. For instance, for one-step evolutions, by considering the condition $u_{0,0}^* u_{1,0} + u_{0,1}^* u_{0,0} = 0$ on the randomly chosen states the fidelity values are all equal to 1. This means that all states satisfying this constraint can be generated via this method. For $d = 4, 9,$ and 16, we find classes of states that can be generated with a mean fidelity over 0.9. A more detailed analysis is presented in Appendix C.

Finally, in order to show the potentiality of the protocol in cryptographic scenarios, we provide a general procedure to generate two mutually unbiased bases (MUBs) in a 2^n-dimensional Hilbert space with a 2DssQW evolution in Appendix D.

IV. EXPERIMENTAL RESULTS

We experimentally realize 2D qudit states by performing single-particle 2DssQWs in the transverse momentum space of a single photon and by projecting the evolved state onto an arbitrary polarization at the end of the evolution. The QW is implemented by using polarization gratings, called g plates [41,61,63]. A g plate adds or subtracts a fixed amount of transverse momentum along a given direction depending on

the polarization of the photon. The action of a g plate on a transverse momentum component k_i can be described as

$$|k_i, R/L\rangle = |k_i \pm \bar{k}, L/R\rangle \qquad (24)$$

where the $|R\rangle$ and $|L\rangle$ are, respectively, the circular right-handed and left-handed polarization, while the direction i and the fixed amount $\bar{k}$ depend on fabrication settings of the plate. The g plates implement the translation operator $\tilde{T}$, defined by Eq. (3), along the directions x and y in transverse momentum space. The coin operators are implemented by using tunable waveplates, i.e., waveplates with tunable optical retardation controlled by an external electric field. The QW evolution is controlled by changing the optical retardation parameters of the tunable waveplates at each step. The scheme of the experimental platform is shown in Fig. 4. Single photons were generated by spontaneous parametric down-conversion process, composed of a nonlinear beta barium borate crystal pumped by a pulsed laser with $\lambda = 392.5$ nm. For each pair of generated photons ($\lambda = 785$ nm), one of them is sent to the QW platform, while the other one is used as a trigger to measure twofold events. After the evolution, a waveplate and a polarizing beamsplitter are used to project the photon state onto an arbitrary polarization. The measurement with coherent light is realized by injecting a coherent laser source (not shown in the experimental setup) at the input of the 2DQW platform. The coherent source is a pulsed laser with a wavelength $\lambda = 785$ nm.

The qudit states are generated by exploiting one-, two-, and three-step QW evolutions. A generic qudit state is given by

$$|\phi_{\text{exp}}\rangle = \sum_{i=0}^{N} \sum_{j=0}^{N} u_{i,j} |i\bar{k}, j\bar{k}\rangle, \qquad (25)$$

where $u_{i,j}$ is the complex amplitude associated with the transverse momentum mode $(k_x, k_y) = (i\bar{k}, j\bar{k})$, which can be written as $u_{i,j} = a_{i,j} e^{i\delta_{i,j}}$, where $a_{i,j}$ is the modulus and $\delta_{i,j}$ is the phase. We use the following notation for the target states:

$$|\phi\rangle = \begin{pmatrix} u_{0,N} & \cdots & u_{N,N} \\ \vdots & \ddots & \vdots \\ u_{0,0} & \cdots & u_{N,0} \end{pmatrix}, \qquad (26)$$
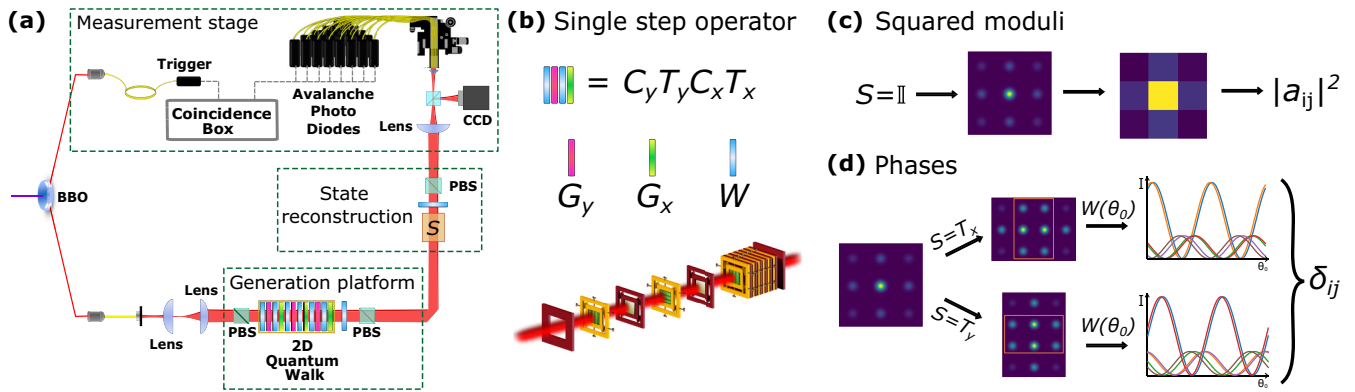
FIG. 4. Platform for qudit generation and state measurement. (a) The generation of the state is performed by evolving the initial Gaussian state with $|H\rangle$ polarization within the 2DssQW platform. The QW is performed in the transverse momentum space by using a cascade of liquid-crystal devices, i.e., g plates along x (G_x), y (G_y), and a waveplate with tunable optical retardation (W), as highlighted in the inset (b). After the evolution, the state is projected onto an arbitrary polarization by using a waveplate and a polarizing beamsplitter. The reconstruction of the state requires determining the probabilities (squared moduli) and the phases of all transverse momentum modes. For squared-modulus measurement, we do not perform any transformation on the state ($S = \mathbb{I}$), as shown in the inset (c). The measurement of the phase difference is accomplished by letting the spots interfere, applying an additional translation, and finally projecting onto a linearly polarized coin. The measurements of squared moduli and the phase differences are performed with classical light with a CCD camera. Classical light was generated by a coherent pulsed laser with $\lambda = 785$ nm. The single-photon measurements were performed by counting twofold coincidence events between "trigger" photons and the evolved "signal" photons generated by the spontaneous parametric down-conversion process. The evolved photons at the output of the reconstruction stage are coupled into a 2D fiber array. Each fiber of the latter is connected to an avalanche photodiode detector. Legend: BBO - Beta Barium Borate, BS - Beam Splitter, PBS - Polarizing Beam Splitter, CCD - Charge Coupled Device.

where $u_{i,j}$ is the complex amplitude of the mode $|i, j\rangle$ of the state $|\phi\rangle$. We benchmark the platform by generating the following qudit states with nine and seven modes, respectively, by exploiting two-step evolutions:

$$|\phi_1\rangle^{(2)} = \frac{1}{2\sqrt{5}}\begin{pmatrix} e^{-i\frac{3}{4}\pi} & \sqrt{2} & e^{i\frac{3}{4}\pi} \\ \sqrt{2} & 2\sqrt{2} & \sqrt{2} \\ e^{i\frac{3}{4}\pi} & \sqrt{2} & e^{-i\frac{3}{4}\pi} \end{pmatrix}, \quad (27)$$

$$|\phi_2\rangle^{(2)} = \frac{1}{\sqrt{10}}\begin{pmatrix} -i & i & 0 \\ 1 & 2 & 1 \\ 0 & i & -i \end{pmatrix}. \quad (28)$$

The chosen states fulfill Eq. (23) as well as the constraints in Eqs. (13)–(15). We experimentally realize these states by using coherent light and single photons. Then, we generate two complete bases belonging to a set of two MUBs in a four-dimensional qudit Hilbert space by using coherent light. We can represent the computational basis $\{|\phi_i\rangle^{(M)}\}$ and the basis $\{|\tilde{\phi}_i\rangle^{(M)}\}$ as

$$|\phi_1\rangle^{(M)} = \begin{pmatrix} 0 & 0 \\ 1 & 0 \end{pmatrix}, \quad |\phi_2\rangle^{(M)} = \begin{pmatrix} 0 & 1 \\ 0 & 0 \end{pmatrix},$$

$$|\phi_3\rangle^{(M)} = \begin{pmatrix} 0 & 0 \\ 0 & 1 \end{pmatrix}, \quad |\phi_4\rangle^{(M)} = \begin{pmatrix} 1 & 0 \\ 0 & 0 \end{pmatrix}, \quad (29)$$

$$|\tilde{\phi}_1\rangle^{(M)} = \frac{1}{2}\begin{pmatrix} i & 1 \\ 1 & i \end{pmatrix}, \quad |\tilde{\phi}_2\rangle^{(M)} = \frac{1}{2}\begin{pmatrix} i & -1 \\ 1 & -i \end{pmatrix},$$

$$|\tilde{\phi}_3\rangle^{(M)} = \frac{1}{2}\begin{pmatrix} i & 1 \\ -1 & -i \end{pmatrix}, \quad |\tilde{\phi}_4\rangle^{(M)} = \frac{1}{2}\begin{pmatrix} i & -1 \\ -1 & i \end{pmatrix}. \quad (30)$$

Final measurements concern the generation of three qudit states with coherent light by exploiting three-step QW

evolutions. The detailed list of these states is reported in Appendix E1.

The fidelity $\mathcal{F}$ between the target $|\phi_{\text{tar}}\rangle$ and experimental states $|\phi_{\text{exp}}\rangle$ is defined as

$$\mathcal{F} = |\langle\phi_{\text{tar}}|\phi_{\text{exp}}\rangle|^2. \quad (31)$$

This value quantifies the accuracy of the generation of the target state. To compute this quantity, we need to fully reconstruct the experimental state. Hence, we measure the squared moduli of the amplitudes $|a_{i,j}|^2$ and the differences between the phases $\delta_{i,j}$ of adjacent modes of each experimental state.

A. State reconstruction

In the following, we describe in detail the complete analysis for two chosen states ($|\phi_1\rangle^{(2)}$ and $|\phi_2\rangle^{(2)}$), performed with coherent light and single-photon events. The squared moduli of the amplitudes $|a_{i,j}|^2$ are measured by setting the transformation S in Fig. 4(a) equal to the identity, as shown in Fig. 4(c). They can be measured by mapping the transverse momentum modes into spatially separated modes. This transformation is performed by a convex lens on the focal plane. For classical light, the intensity of each spatial mode is proportional to the squared moduli of the amplitudes $|a_{i,j}|^2$ of the corresponding transverse momentum mode (i, j). The intensity pattern can be retrieved by using a CCD camera. In the single-photon regime, the squared moduli of the amplitudes $|a_{i,j}|^2$ is proportional to the number of photons in the transverse momentum mode (i, j). In this case, measurements are performed by coupling each mode into a 2D-multimode fiber array. The uncertainties on the squared moduli are obtained by considering a Poissonian statistic for the photon counting process. Each fiber is connected to an avalanche photodiode detector (APD). The squared modulus value of each mode is
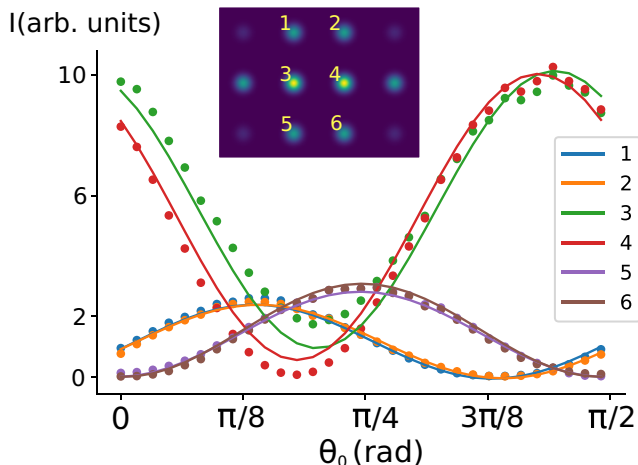
FIG. 5. Intensity of the intermediate modes as a function of the angle θ_0. We report as an example the variation of intensity of the intermediate modes vs the inclination of the half-wave plate optic angle θ_0 by using coherent light. The intermediate modes are generated by applying a g plate along the x direction at the output of the QW platform. In this way, the horizontal adjacent modes interfere in the intermediate modes. Then, all the modes are projected on a linear polarization by using a half-wave plate with optical angle θ_0 and a polarizing beamsplitter. The intensities of modes depend on θ_0 as $I \propto -\cos(4\theta_0 - \Delta\delta_{i,j}^{(x)})$. In the inset, a real picture of intermediate modes is reported. The numeration on the inset allows one to recognize the corresponding curve in the graphics. The intensity values are reported in arbitrary units.

proportional to the number of photons counted in that mode. We count only the twofold events, i.e., the photons detected by the APD at the same time of the trigger photon.

The measurement of the phase differences between adjacent modes of the experimental states is performed by setting the transformation S equal to a translation T along x and y, as shown in Fig. 4(d). Experimentally, these translations are performed by a g plate along x and y, respectively. These further transformations move at the same site as the modes that

are adjacent along horizontal and vertical directions, respectively. As an example, we consider the adjacent modes $|i, j\rangle$ and $|i + 1, j\rangle$ and the respective amplitudes $u_{i,j}$ and $u_{i+1,j}$. These two amplitudes interfere on an intermediate mode by applying a g plate along x. By using a half-wave plate rotated θ_0 degrees and a polarizing beamsplitter, we project this mode on a generic linear polarization inclined by $2\theta_0$ with respect to the horizontal polarization:

$$|2\theta_0\rangle = \frac{1}{\sqrt{2}}|R\rangle + \frac{e^{i4\theta_0}}{\sqrt{2}}|L\rangle. \tag{32}$$

After the projection, the intensity value of the intermediate mode is proportional to

$$I(\theta_0) \propto -\cos\left(4\theta_0 + \Delta\delta_{i,j}^{(x)}\right), \tag{33}$$

where $\Delta\delta_{i,j}^{(x)}$ is the phase difference $\delta_{i,j} - \delta_{i+1,j}$ between the mode (i, j) and $(i + 1, j)$. Hence, the intensity as a function of θ_0 allows us to directly measure the value $\Delta\delta_{i,j}^{(x)}$ with the respective error. The same procedure allows measuring the value $\Delta\delta_{i,j}^{(y)}$ by setting the transformation S as T_y, implemented by a g plate along y. In Fig. 5, the intensities of the intermediate modes are provided as function of θ_0 by using coherent light, when considering the target state $|\phi_1\rangle^{(2)}$. The phase differences are exploited to obtain the value of the phases $\delta_{i,j}$ with their errors, as shown in Appendix E2. We calculate the phase distribution for the states generated with coherent light and with single photons. The distributions of squared moduli and phases for the states $|\phi_1\rangle^{(2)}$ and $|\phi_2\rangle^{(2)}$ in classical and single-photon regimes are shown in Fig. 6.

B. Fidelity measurement

We calculate the value of the fidelity resulting from the experimental evolutions [see Eq. (31)] (1) $\mathcal{F}_1^{(c)} = 0.974 \pm 0.003$ and $\mathcal{F}_2^{(c)} = 0.981 \pm 0.002$ using coherent light and (2) $\mathcal{F}_1^{(q)} = 0.9849 \pm 0.0008$ and $\mathcal{F}_2^{(q)} = 0.9723 \pm 0.0008$ using single-photon inputs, where the indices 1 and 2 refer, respectively, to the states $|\phi_1\rangle^{(2)}$ and $|\phi_2\rangle^{(2)}$. We evaluated the
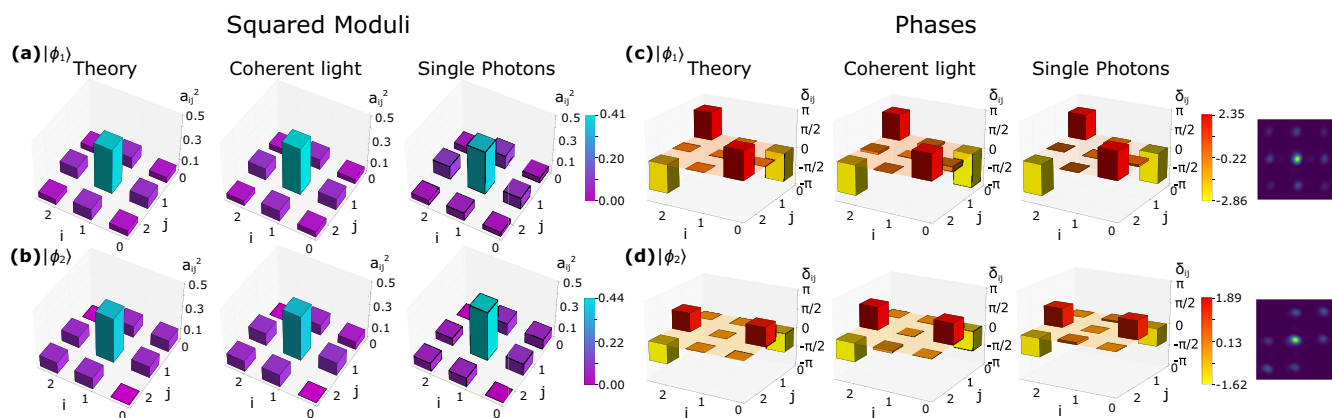

FIG. 6. Theoretical and experimentally reconstructed values of squared moduli and phases of two states generated by the 2DQW platform. Theoretical and experimental reconstruction of squared moduli and phases relative to the states $|\phi_1\rangle^{(2)}$ (a), (c) and $|\phi_2\rangle^{(2)}$ (b), (d), defined in Eqs. (27) and (28). The reported experimental data are obtained by using both coherent light and single-photon acquisition. For single-photon acquisition, the error bars are calculated by bootstrapping approach. Error bars are too small to be visible. On the right, we report the intensity distribution as it appears on the CCD camera.

TABLE I. The fidelity values of the generated states that belong to a set of MUBs in a four-dimensional Hilbert state, where $|\phi_i\rangle^{(M)}$ is the standard computational basis defined in Eq. (29) and $|\tilde{\phi}_i\rangle^{(M)}$ is defined in Eq. (30).

State	Fidelity ($\mathcal{F}^{(c)}$)	State	Fidelity ($\mathcal{F}^{(c)}$)
$|\phi_1\rangle^{(M)}$	0.9936 ± 0.0004	$|\tilde{\phi}_1\rangle^{(M)}$	0.9645 ± 0.0011
$|\phi_2\rangle^{(M)}$	0.9944 ± 0.0003	$|\tilde{\phi}_2\rangle^{(M)}$	0.9987 ± 0.0009
$|\phi_3\rangle^{(M)}$	0.9955 ± 0.0004	$|\tilde{\phi}_3\rangle^{(M)}$	0.9892 ± 0.0008
$|\phi_4\rangle^{(M)}$	0.9958 ± 0.0002	$|\tilde{\phi}_4\rangle^{(M)}$	0.975 ± 0.002

uncertainties on the fidelity through a bootstrapping approach. These values of fidelity show a good agreement between target and experimental states. We can also note a remarkable agreement between the measurements performed with coherent light and single photons, which confirms the stability and reliability of our experimental platform.

We realize the computational basis $\{|\phi_i\rangle^{(M)}\}$ and the basis $\{|\psi_i\rangle^{(M)}\}$ defined above. In Table I, we report the obtained fidelities. Finally, we generate qudit states with coherent light by exploiting three steps of a 2DQW evolution. These states are reported in Appendix E1 and correspond to 16, 14, and 8 modes, respectively. Table II reports the obtained values of the mean fidelity between the target and the experimental states.

V. CONCLUSIONS AND DISCUSSION

In conclusion, we demonstrate that 2DQWs with a two-level coin are a useful tool for the generation of a subset of high-dimensional quantum states. We theoretically prove that the nonuniversality of 2DQW derives from the quadratic increase in dimension of the Hilbert space of the output states at each step. On the other hand, this scaling permits the generation of high-dimensional states by using less resources with respect to the 1DQW.

We experimentally implement a set of quantum states belonging to the subset of states which fulfill the conditions in Eqs. (13)–(15). Here, we demonstrate the feasibility of the platform to manipulate the transverse momentum of the output photons. We exploit coherent-light and single-photon sources, obtaining similar results for the target states $|\phi_1\rangle^{(2)}$ and $|\phi_2\rangle^{(2)}$. Moreover, we experimentally proved the potential of our protocol for applications in quantum cryptography by showing a procedure that allows one to generate two bases belonging to a set of MUBs in the 2^n-dimensional Hilbert space.

TABLE II. The fidelity values of the generated states using three steps of QW. The state reconstructions are performed by using coherent light. The list of generated states is reported in Appendix E1.

State	Modes	Fidelity ($\mathcal{F}^{(c)}$)
$|\phi_1\rangle^{(3)}$	16	0.943 ± 0.003
$|\phi_2\rangle^{(3)}$	14	0.855 ± 0.003
$|\phi_3\rangle^{(3)}$	8	0.9842 ± 0.0006

This paper provides insight towards the generation of single-particle high-dimensional states, that have already found large applications in quantum cryptography and quantum information protocols [65–68]. By exploiting a platform that encodes the spatial dimension in two independent degrees of freedom, it is possible to generate qudit states with intraparticle hybrid correlations between different degrees of freedom. In parallel, further prospects of this paper involve a full characterization of 2DQW dynamics when injected with multiparticle input states [62], to investigate the potential of multiqudit state generation via this platform. This finds a straightforward application in the field of secure quantum communication protocols, requiring the implementation of complex entangled qudit states. Indeed, spanning Hilbert spaces of greater dimensions allows for improved information capacity and noise resilience, leading to enhanced quantum information processing. In general, these kinds of states find applications in several quantum information fields beyond quantum communication [46,69–73].

APPENDIX A: CONDITIONS FOR THE 2DSSQW OUTPUT STATES

Here we show the action of split-step operators $U_{x,1}$, $U_{y,1}$, and $U_{x,2}$ on an initial state localized at the $(0,0)$ position of the lattice with a generic coin state. This analysis allows recognizing the conditions for the output states evolved by the initial three split-step evolution, and generalizing these constraints to the output states evolved by N single-step evolutions. The states that can be realized by 2DssQW evolutions represent a subset of the total Hilbert space, hence we provide a characterization for the subsets of one-, two-, and three-step evolution. Finally, we show the procedure to reconstruct an evolution of the 2DssQW of the output states that belong to the subset.

The first split-step evolution is obtained by applying the operator $U_{x,1} = T_x C_{x,1}$ to the seed state $|\psi_0\rangle$. We consider the initial state $|\psi_0\rangle$ as the following *seed* state:

$$|\psi_0\rangle = u_{0,0,\uparrow}^{(0)} |0, 0, \uparrow\rangle + u_{0,0,\downarrow}^{(0)} |0, 0, \downarrow\rangle, \qquad (A1)$$

i.e., a localized state in the position $(0,0)$ of the lattice with a generic coin state. The coin operator $C_{x,1}$ rotates the coin state into another generic superposition. Then, the translation operator T_x moves to the left the $|\downarrow\rangle$ coin element and flips it over. Similarly, the coin element $|\uparrow\rangle$ is translated to the right and flipped. For this reason, after each $U_{x,i}$ operator, the sites on the right boundary are only populated by $|\downarrow\rangle$ components and the left boundary is only populated by $|\uparrow\rangle$ components. Thus, the state $|\varphi_1\rangle$ is given by

$$|\varphi_1\rangle = U_{x,1}|\psi_0\rangle = l_{0,0,\uparrow}^{(1)} |0, 0, \uparrow\rangle + l_{1,0,\downarrow}^{(1)} |1, 0, \downarrow\rangle, \qquad (A2)$$
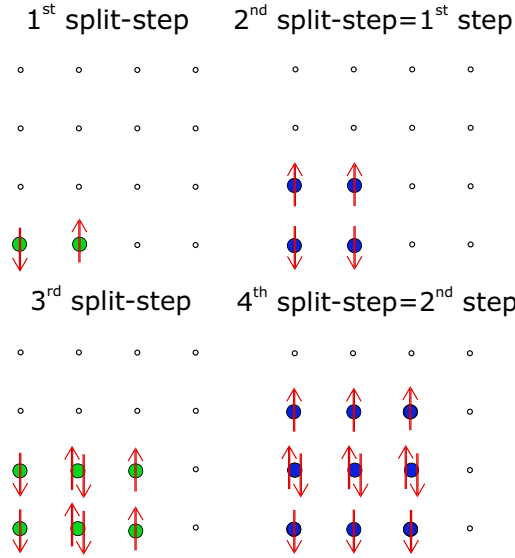
FIG. 7. Pictorial representation of the boundary and scalar product conditions within a 2DQW evolution. Four split steps representing two steps of the quantum walk are depicted. Red arrows on each lattice site represent the coin state of the site after $U_{x,i}$ or $U_{y,i}$ operation. At each $U_{x,i}$ evolution (green spots) the states of the lattice sites at the left (right) boundary only present $|\downarrow\rangle$($|\uparrow\rangle$) components. Equivalently, after each $U_{y,i}$ evolution (blue spots) the states of the lattice sites at the bottom (top) boundary only present $|\downarrow\rangle$($|\uparrow\rangle$) components [see Eq. (5)].

and the two boundary conditions follow:

$$l_{0,0,\downarrow}^{(1)} = 0, \quad l_{1,0,\uparrow}^{(1)} = 0. \tag{A3}$$

By considering Eqs. (10) and (11), the state in Eq. (A2) can be equivalently described by the single vector $\vec{l}_{0,0}^{(1)}$ equal to

$$\vec{l}_{0,0}^{(1)} = \begin{pmatrix} l_{0,0,\uparrow}^{(1)} \\ l_{1,0,\downarrow}^{(1)} \end{pmatrix} = C_{x,1} \begin{pmatrix} u_{0,0,\uparrow}^{(0)} \\ u_{0,0,\downarrow}^{(0)} \end{pmatrix}. \tag{A4}$$

The index of the vector $\vec{l}_{0,0}^{(1)}$ takes into account that both the coefficients $l_{0,0,\uparrow}^{(1)}$ and $l_{1,0,\downarrow}^{(1)}$ come from the same site $(0,0)$ as in the previous step.

We consider the second split-step evolution given by the operator $U_{y,1}$:

$$
\begin{aligned}
|\psi_1\rangle &= U_{y,1}|\varphi_1\rangle \\
&= u_{0,0,\uparrow}^{(1)}|0,0,\uparrow\rangle + u_{0,1,\downarrow}^{(1)}|0,1,\downarrow\rangle \\
&\quad + u_{1,0,\uparrow}^{(1)}|1,0,\uparrow\rangle + u_{1,1,\downarrow}^{(1)}|1,1,\downarrow\rangle. \tag{A5}
\end{aligned}
$$

Using an argument similar to the case of $U_{x,i}$, four boundary conditions arise:

$$u_{0,0,\downarrow}^{(1)} = u_{1,0,\downarrow}^{(1)} = 0, \quad u_{0,1,\uparrow}^{(1)} = u_{1,1,\uparrow}^{(1)} = 0. \tag{A6}$$

In Fig. 7, the boundary conditions for the initial four split steps are graphically represented. The state can be described by two nonzero vectors $\vec{u}_{0,0}^{(1)}$ and $\vec{u}_{1,0}^{(1)}$:

$$\vec{u}_{i,0}^{(1)} = \begin{pmatrix} u_{i,0,\uparrow}^{(1)} \\ u_{i,1,\downarrow}^{(1)} \end{pmatrix} = C_{y,1} \begin{pmatrix} l_{i,0,\uparrow}^{(0)} \\ l_{i,0,\downarrow}^{(0)} \end{pmatrix} \quad \text{with } i = 0, 1. \tag{A7}$$
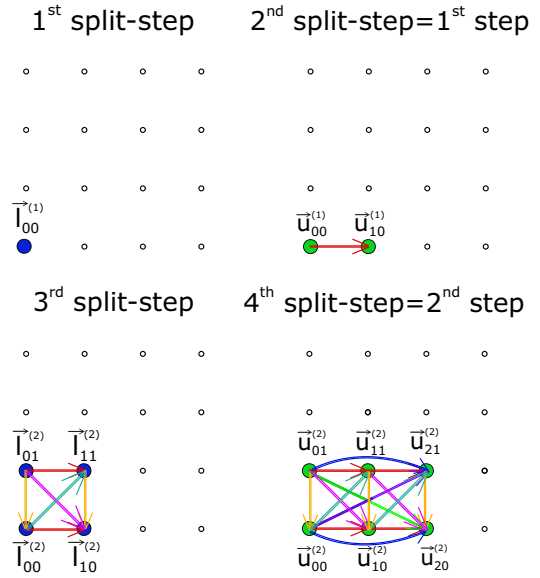

FIG. 8. Pictorial representation of the scalar product conditions within a 2DQW evolution. Scalar product conditions for the first, second, third, and fourth split step are depicted. Each populated position indicates vectors described by Eqs. (10) and (11) for odd and even split steps, respectively. Each arrow represents the scalar products between the two vectors at the tail and at the head of the arrow. For the first split step we have only one vertex, hence there is no scalar product condition. For the second split step, the two vertices are connected by one arrow. The first condition [see Eq. (A8)] is obtained by setting to zero the scalar product represented by the arrow. At the third split step, the conditions represented by the arrows increase. All the scalar products represented by parallel arrows of the same length have to be summed and zeroed.

It is worth noticing that the number of nonzero vectors that describes the walker state is always equal to the number of populated sites in the previous split step. From the boundary conditions of the first split step [see Eq. (A3)], it immediately follows that

$$\vec{u}_{0,0}^{(1)\dagger} \cdot \vec{u}_{1,0}^{(1)} = 0. \tag{A8}$$

Indeed, the boundary conditions in Eq. (A3) allow us to write

$$\vec{u}_{0,0}^{(1)} = C_{y,1} \begin{pmatrix} l_{0,0,\uparrow}^{(0)} \\ 0 \end{pmatrix}, \quad \vec{u}_{1,0}^{(1)} = C_{y,1} \begin{pmatrix} 0 \\ l_{1,0,\downarrow}^{(0)} \end{pmatrix}. \tag{A9}$$

The vectors before the transformation $C_{y,1}$ are orthogonal. Since $C_{y,1}$ is a unitary transformation, the orthogonality is preserved for the transformed vectors. This condition is graphically depicted in Fig. 8, where the arrow between two sites indicates that the scalar product between two vectors is zero. It is straightforward to reconstruct the scalar product conditions by just considering the graph of populated sites in the previous split step. The third split step $|\varphi_2\rangle = U_{x,2}|\psi_2\rangle$ can be described by the four nonzero vectors:

$$\vec{l}_{i,j}^{(2)} = \begin{pmatrix} l_{i,j,\uparrow}^{(2)} \\ l_{i+1,j\downarrow}^{(2)} \end{pmatrix} = C_{x,2} \begin{pmatrix} u_{i,j,\uparrow}^{(1)} \\ u_{i,j,\downarrow}^{(1)} \end{pmatrix}, \tag{A10}$$

(a) Third step

18 conditions

(b) Fourth step

32 conditions

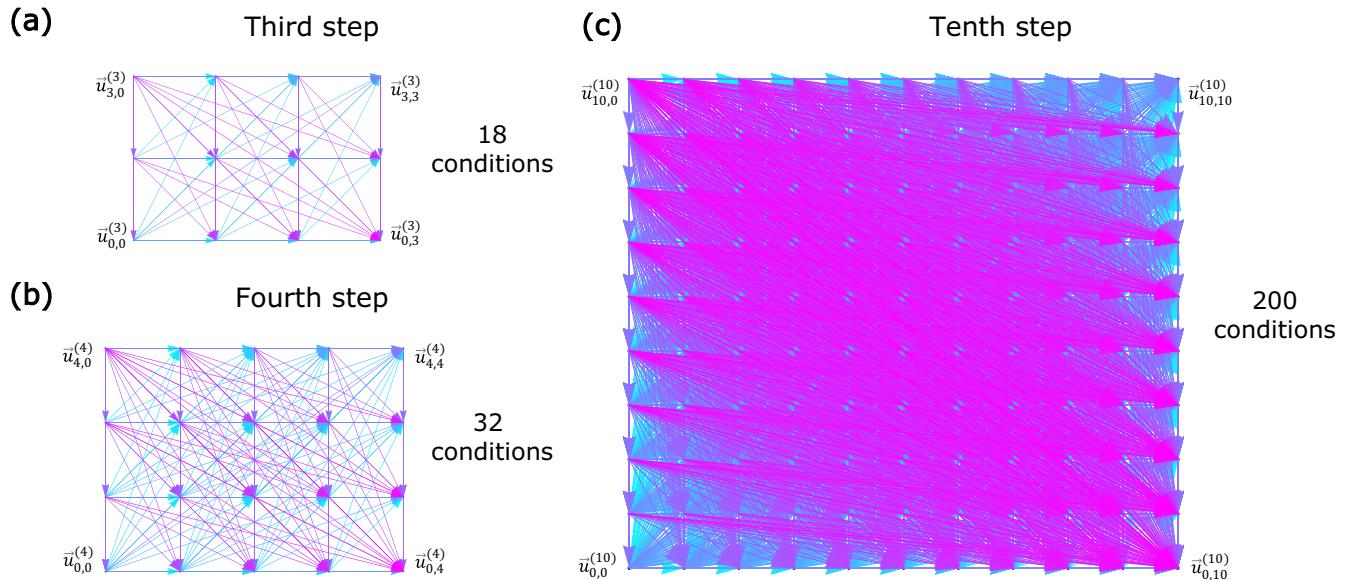**(c)** Tenth step

200 conditions

FIG. 9. Constraints on the amplitude coefficients when increasing the number of steps. The arrows represent the constraints and the colors are related to the arrow length. The number of associated constraints increases quadratically with the number of steps. The number of independent parameters of the coin operators increases linearly instead, thus limiting the space of states to be realized. Number of conditions: (a) 18 (three steps), (b) 32 (four steps), and (c) 200 (ten steps).

where i and j can assume the integer values $[0,1]$. The boundary conditions are obtained from the action of the operator $U_{x,2}$ and are given by

$$l_{0,0,\downarrow}^{(2)} = l_{2,0,\downarrow}^{(2)} = 0,$$
$$l_{0,1,\uparrow}^{(2)} = l_{2,1,\uparrow}^{(2)} = 0. \tag{A11}$$

We can obtain three scalar-product conditions for the output state at the third split step $|\varphi_2\rangle$ by using the same argument as in the previous split step:

$$\vec{l}_{0,0}^{(2)\dagger} \cdot \vec{l}_{1,1}^{(2)} = \vec{l}_{0,1}^{(2)\dagger} \cdot \vec{l}_{1,0}^{(2)} = 0,$$
$$\vec{l}_{0,1}^{(2)\dagger} \cdot \vec{l}_{0,0}^{(2)} = \vec{l}_{1,1}^{(2)\dagger} \cdot \vec{l}_{1,0}^{(2)} = 0. \tag{A12}$$

A further condition can be derived through Eq. (A8):

$$0 = \vec{u}_{0,0}^{(1)\dagger} \cdot \vec{u}_{1,0}^{(1)} = u_{0,0,\uparrow}^{(1)*} u_{1,0,\uparrow}^{(1)} + u_{0,1,\downarrow}^{(1)*} u_{1,1,\downarrow}^{(1)}. \tag{A13}$$

By considering the boundary conditions provided by the first step described in Eq. (A6), we can add the null quantities $u_{0,0,\downarrow}^{(1)*} u_{1,0,\downarrow}^{(1)} + u_{0,1,\uparrow}^{(1)*} u_{1,1,\uparrow}^{(1)}$:

$$u_{0,0,\uparrow}^{(1)*} u_{1,0,\uparrow}^{(1)} + u_{0,1,\downarrow}^{(1)*} u_{1,1,\downarrow}^{(1)} + u_{0,0,\downarrow}^{(1)*} u_{1,0,\downarrow}^{(1)} + u_{0,1,\uparrow}^{(1)*} u_{1,1,\uparrow}^{(1)} = 0.$$

By recalling the definitions provided in Eq. (10), we obtain

$$\vec{l}_{0,0}^{(2)\dagger} \cdot \vec{l}_{1,0}^{(2)} + \vec{l}_{0,1}^{(2)\dagger} \cdot \vec{l}_{1,1}^{(2)} = 0, \tag{A14}$$

by using $C_{x,2} C_{x,2}^{\dagger} = \mathbb{I}$. All the conditions for the third split step are graphically depicted in Figs. 7 and 8. In Fig. 8, we can recognize each arrow as a scalar product between two vectors represented by the vertices. We reconstruct the constraints in Eq. (A12) by reducing to zero the scalar product represented by the vertical and diagonal arrows. In order to obtain the constraints in Eq. (A14), we sum up the scalar products represented by the horizontal arrows in the same graph.

Starting from the graphical representation of the conditions, we obtain the condition for the output states after N single-step evolutions [see Eqs. (13)–(18)]. In Fig. 9, the conditions for the third, fourth, and tenth step are graphically depicted. The number of conditions increases quadratically with the number of steps, as opposed to the number of independent parameters, increasing linearly with the number of steps. For this reason, it is not possible to realize an arbitrary state in the two-dimensional walker space.

APPENDIX B: SET OF COIN OPERATORS GENERATING A STATE

Here, we explain how to derive the coin operators that generate the state $|\psi_N\rangle$ at any even split step $2M = N$. The output state of a 2DssQW at the Nth step satisfies the constraints of Eqs. (13)–(15). In order to find the coin operators that generate this state, we focus on one of the two constraints corresponding to $h = N$ and $k = N - 1$:

$$\vec{u}_{0,0}^{(N)\dagger} \cdot \vec{u}_{N,N-1}^{(N)} = 0, \quad \vec{u}_{0,N-1}^{(N)\dagger} \cdot \vec{u}_{N,0}^{(N)} = 0. \tag{B1}$$

To find the coin operator $C_{y,N}$, we can choose one of these two equations. By considering the first equation, the vector $\vec{u}_{0,0}^{(N)}$ and $\vec{u}_{N,N-1}^{(N)}$ can be written as

$$\vec{u}_{0,0}^{(N)} = C_{y,N} \begin{pmatrix} l_{0,0,\uparrow}^{(N)} \\ 0 \end{pmatrix},$$

$$\vec{u}_{N,N-1}^{(N)} = C_{y,N} \begin{pmatrix} 0 \\ l_{N,N-1,\downarrow}^{(N)} \end{pmatrix}, \tag{B2}$$

where $l_{0,0,\downarrow}^{(N)} = l_{N,N-1,\uparrow}^{(N)} = 0$ for the boundary condition of the previous split step, thus implying the following equations for

the coin operator:

$$C_{y,N}^\dagger \vec{u}_{0,0}^{(N)} = \begin{pmatrix} l_{0,0,\uparrow}^{(N)} \\ 0 \end{pmatrix},$$

$$C_{y,N}^\dagger \vec{u}_{N,N-1}^{(N)} = \begin{pmatrix} 0 \\ l_{N,N-1,\downarrow}^{(N)} \end{pmatrix}. \tag{B3}$$

The coin operator $C_{y,N}$ is a generic 2×2 matrix:

$$C_{y,N} = \begin{pmatrix} a_1 & b_1 \\ a_2 & b_2 \end{pmatrix}. \tag{B4}$$

From Eq. (B3) it follows that

$$\vec{b}^\dagger \cdot \vec{u}_{0,0}^{(N)} = 0, \quad \vec{a}^\dagger \cdot \vec{u}_{N,N-1}^{(N)} = 0, \tag{B5}$$

with $\vec{a} = (a_1, a_2)$ and $\vec{b} = (b_1, b_2)$. By merging these equations with Eq. (B1), we can directly deduce

$$\vec{a} = e^{i\beta} \vec{u}_{0,0}^{(N)}, \quad \vec{b} = e^{i\alpha} \vec{u}_{N,N-1}^{(N)}. \tag{B6}$$

A quantum state is defined up to a global phase, hence we can set $\beta = 0$ and the coin operator becomes

$$C_{y,N} = \begin{pmatrix} u_{0,0,\uparrow}^{(N)} & e^{i\alpha} u_{N,N-1,\uparrow}^{(N)} \\ u_{0,1,\downarrow}^{(N)} & e^{i\alpha} u_{N,N,\downarrow}^{(N)} \end{pmatrix}. \tag{B7}$$

The coin operator is defined up to a relative phase between the first and the second column. Hence, the evolution that permits us to reproduce the designed final state $|\psi_N\rangle$ is not unique. The second equation in Eq. (B1) leads to the same results for $C_{y,N}$.

By applying the operator $U_{y,N}^\dagger = C_{y,N}^\dagger T_y^\dagger$ to the state $|\psi_N\rangle$ we obtain the state $|\varphi_N\rangle$ corresponding to the split step $2M - 1$. It satisfies all the constraints of an odd split-step quantum walk state. In particular, we focus on

$$\vec{l}_{0,0}^{(N)\dagger} \cdot \vec{l}_{N-1,N-1}^{(N)} = 0, \quad \vec{l}_{0,N-1}^{(N)\dagger} \cdot \vec{l}_{N-1,0}^{(N)} = 0. \tag{B8}$$

Using the same argument as $2M$ split steps, we can obtain the coin operator $C_{x,N}$ as

$$C_{x,N} = \begin{pmatrix} l_{0,0,\uparrow}^{(N)} & e^{i\alpha} l_{N-1,N-1,\uparrow}^{(N)} \\ l_{1,0,\downarrow}^{(N)} & e^{i\alpha} l_{N,N-1,\downarrow}^{(N)} \end{pmatrix}. \tag{B9}$$

These arguments can be applied back to the first split step. Indeed, there is no constraint equation at this split step. For this reason, the coin operator is calculated directly by imposing

$$\begin{pmatrix} u_{0,0,\uparrow}^{(0)} \\ u_{0,0,\downarrow}^{(0)} \end{pmatrix} = C_{x,1}^\dagger \begin{pmatrix} l_{0,0,\uparrow}^{(1)} \\ l_{1,0,\downarrow}^{(1)} \end{pmatrix}. \tag{B10}$$

In conclusion, we can reconstruct the whole QW evolution that allows one to obtain a given output state.

APPENDIX C: CHARACTERIZATION OF THE SUBSET

Two-dimensional quantum walk protocols allow generating states that belong to a subset of the whole Hilbert space. In Sec. III C of the main text, we give a numerical characterization of this subset. It consists in the calculation of the

fidelity between a randomly chosen state and the best approximation of this state given by the output state of the quantum walk. Here, by following the same principle, we calculate the fidelity values by considering more stringent conditions on the randomly chosen states for the two- and three-step evolution. In Fig. 10, we report different histograms of fidelity values by imposing different conditions on randomly chosen qudits with dimensions $d = 9$ and 16.

APPENDIX D: GENERATION OF MUTUALLY UNBIASED BASES IN A *D*-DIMENSIONAL HILBERT SPACE

Here, we provide a procedure to generate a basis $|\psi_i^{(n)}\rangle$ that is mutually unbiased with the computational basis $|e_{l,m}^{(n)}\rangle$, i.e.,

$$\left|\langle \psi_i^{(n)} | e_{l,m}^{(n)} \rangle\right| = \frac{1}{\sqrt{d}} \tag{D1}$$

where $d = 2^n$ is the dimension of the Hilbert space. The computational basis is defined as

$$|e_{l,m}\rangle = \sum_{i=0}^N \sum_{j=0}^N \delta_{i,l} \delta_{j,m} |i, j\rangle. \tag{D2}$$

The vectors of the computational basis satisfy the conditions given by Eqs. (13) and (14). Hence, it is possible to generate the computational basis for each dimension N^2 where N is the number of steps.

The procedure to generate the vectors $|\psi_i^{(n)}\rangle$ consists in applying an evolution operator $U^{(n)}$ on the initially localized state $|\psi_0\rangle = |0, 0\rangle |\uparrow\rangle$ and then projecting the evolved state onto the coin $|+\rangle$, given by $(|\uparrow\rangle + |\downarrow\rangle)/\sqrt{2}$, in the following equation:

$$\left|\psi_i^{(n)}\right\rangle = \langle +|U^{(n)}|\psi_0\rangle. \tag{D3}$$

The operators $U^{(n)}$ are composed by the single-step operators, defined as follows: (1) $U_{\boxtimes}(\zeta_x, \zeta_y)$ that lead to the evolution of both states $|i, j\rangle |\uparrow\rangle$ and $|i, j\rangle |\downarrow\rangle$ in a balanced superposition of four different localized states on the lattice sites; (2) $U_{\searrow}(\zeta_x)$ and $U_{\nearrow}(\zeta_x)$ that evolve the state $|i, j\rangle |\uparrow\rangle$ along the diagonal and the antidiagonal axes with opposite coin states $|\uparrow\rangle$ and $|\downarrow\rangle$; and (3) $U_{\nearrow}$, $U_{\nwarrow}$, $U_{\searrow}$, and $U_{\swarrow}$ that correspond to shifting the localized state $|i, j\rangle |\uparrow\rangle$ along the diagonal and antidiagonal axes in the four directions. Note that the same operators translate the state $|i, j\rangle |\downarrow\rangle$ exactly in the opposite direction. The actions of the operators are shown in Fig. 11. The parameters of the coin operators for each single-step operator defined above are given in Table III.

For $n = 2$, the dimension of the basis is $d = 2^2 = 4$ and the operator $U^{(2)}$ is given by the operator $U_{\boxtimes}(\zeta_x, \zeta_y)$. The spatial distribution of the basis vectors on the lattice is reported in Fig. 12(a). Four different basis vectors are generated when each of the parameters ζ_x and ζ_y takes values $-\pi/2$ and $\pi/2$ according to Table IV. For $d = 2^3 = 8$, operator $U^{(3)}$ is given by

$$U^{(3)} = U_o(\zeta_x^{(2)}) U_{\boxtimes}(\zeta_x^{(1)}, \zeta_y), \tag{D4}$$

where $U_o(\zeta_x^{(2)}) = U_{\searrow} U_{\swarrow}(\zeta_x^{(2)})$. The spatial distribution of the basis vectors on the lattice is reported in Fig. 12(b). The eight basis vectors are generated when each of these parameters
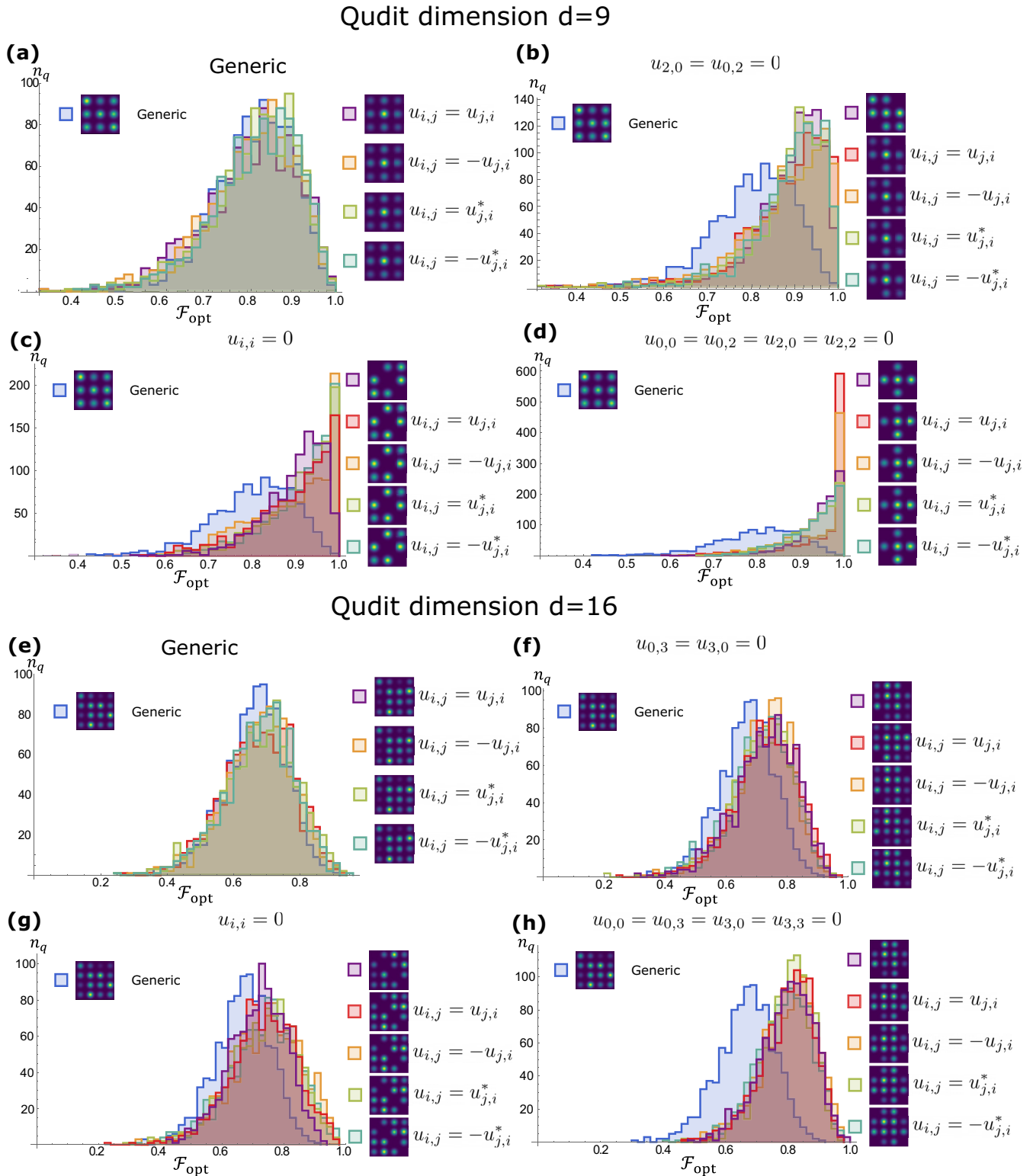
FIG. 10. Histograms of fidelity values for qudit states generated by two and three steps of 2DssQW evolutions. We calculate the fidelity between 1000 randomly chosen qudit states and the best approximation of the states that it is possible to generate by using a 2DssQW evolution and collect the obtained values into histograms for qudit dimension $d = 9$ [(a)–(d)] and $d = 16$ [(e)–(h)]. To further improve the mean fidelity, we tighten the requirement for each condition considered in Fig. 3. We observe that the histograms in the insets (a), (b), and (e)–(h) do not significantly change by imposing more stringent constraints. On the other hand, in insets (c) and (d), the mean fidelity values increase if we impose the same conditions for the states.

(a) Localized state   (b) $U_{\times}$

(c) $U_{\searchrow}$ $U_{\diagup}$ (d) $U_{\searchrow} U_{\diagup} U_{\nwarrow} U_{\diagup}$
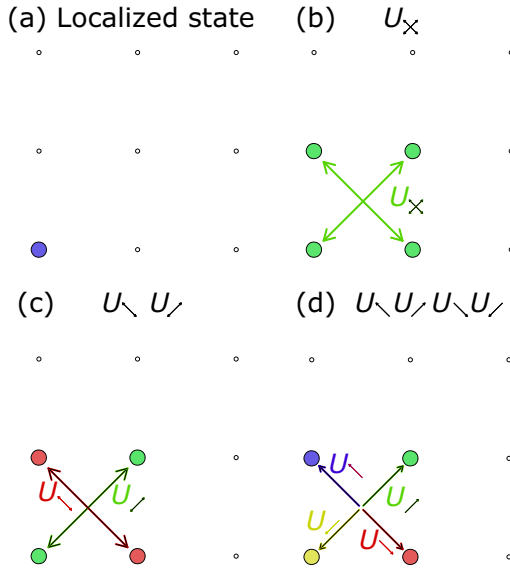
FIG. 11. Action of the single-step operators. Here, we sketch the action of the single-step operators $U_{\times}(\zeta_x, \zeta_y)$ (b), $U_{\searchrow}(\zeta_x)$ (c), and $U_{\diagup}(\zeta_x)$, $U_{\nearrow}$, $U_{\nwarrow}$, $U_{\searchrow}$, and $U_{\diagup}$ (d) on the localized state $|\psi_0\rangle = |0, 0\rangle|\uparrow\rangle$ (a). The operators $U_{\times}(\zeta_x, \zeta_y)$, $U_{\searchrow}(\zeta_x)$, and $U_{\diagup}(\zeta_x), U_{\nearrow}$ evolve the state on a superposition of states localized in different positions with orthogonal coin. The operators $U_{\diagup}(\zeta_x)$, $U_{\nearrow}$, $U_{\nwarrow}$, $U_{\searchrow}$, and $U_{\diagup}$ only shift the state on a new adjacent position.

TABLE III. Coin parameters of the single-step operators. Starting from the definition of the single-step operator $U = U_y U_x$ and from the relative coin operator in Eq. (4), we provide the values for the parameters of the coin that allow us to realize the single-step operators $U_{\times}(\zeta_x, \zeta_y)$, $U_{\searchrow}(\zeta_x)$, $U_{\diagup}(\zeta_x)$, $U_{\nearrow}$, $U_{\nwarrow}$, $U_{\searchrow}$, and $U_{\diagup}$. These operators are fundamental to illustrate the procedure generating a 2^n-dimensional basis which is mutually unbiased with the computational one.

Operators	ξ_x	ζ_x	θ_x	ξ_y	ζ_y	θ_y
$U_{\times}$	0	ζ_x	$\pi/4$	0	ζ_y	$\pi/4$
$U_{\searchrow}$	0	ζ_x	$\pi/4$	0	$-\pi/2$	$\pi/2$
$U_{\diagup}$	0	ζ_x	$\pi/4$	0	0	0
$U_{\nearrow}$	0	$-\pi/2$	$\pi/2$	0	0	0
$U_{\nwarrow}$	0	0	0	0	$-\pi/2$	$\pi/2$
$U_{\searchrow}$	0	$-\pi/2$	$\pi/2$	0	$-\pi/2$	$\pi/2$
$U_{\diagup}$	0	0	0	0	0	0

TABLE IV. Four different basis vectors are obtained when each of the parameters ζ_x and ζ_y takes values $-\pi/2$ or $\pi/2$.

$|\psi_i^{(2)}\rangle$	$\zeta_x^{(1)}$	ζ_y
$|\psi_1^{(2)}\rangle$	$-\frac{\pi}{2}$	$-\frac{\pi}{2}$
$|\psi_2^{(2)}\rangle$	$-\frac{\pi}{2}$	$\frac{\pi}{2}$
$|\psi_3^{(2)}\rangle$	$\frac{\pi}{2}$	$-\frac{\pi}{2}$
$|\psi_4^{(2)}\rangle$	$\frac{\pi}{2}$	$\frac{\pi}{2}$

TABLE V. Eight different basis vectors are obtained when each of the parameters ζ listed takes values $-\pi/2$ or $\pi/2$.

$|\psi_i^{(3)}\rangle$	$\zeta_x^{(1)}$	$\zeta_x^{(2)}$	ζ_y
$|\psi_1^{(3)}\rangle$	$-\frac{\pi}{2}$	$-\frac{\pi}{2}$	$-\frac{\pi}{2}$
$|\psi_2^{(3)}\rangle$	$-\frac{\pi}{2}$	$-\frac{\pi}{2}$	$\frac{\pi}{2}$
$\vdots$	$\vdots$	$\vdots$	$\vdots$
$|\psi_7^{(3)}\rangle$	$\frac{\pi}{2}$	$\frac{\pi}{2}$	$-\frac{\pi}{2}$
$|\psi_8^{(3)}\rangle$	$\frac{\pi}{2}$	$\frac{\pi}{2}$	$\frac{\pi}{2}$

$\zeta_x^{(1)}$, $\zeta_x^{(2)}$, and ζ_y takes values $-\pi/2$ and $\pi/2$ according to Table V. For $d = 2^4 = 16$, the operator $U^{(4)}$ is given by

$$U^{(4)} = U_e\big(\zeta_x^{(3)}\big)U^{(3)} \tag{D5}$$

where $U_e(\zeta_x^{(3)}) = U_{\nearrow}U_{\nwarrow}(\zeta_x^{(3)})$. The spatial distribution of the basis vectors on the lattice is reported in Fig. 12(c). The 16 basis vectors are generated when each parameter $\zeta_x^{(1)}$, $\zeta_x^{(2)}$, $\zeta_x^{(3)}$, and ζ_y takes values $-\pi/2$ and $\pi/2$ according to Table VI. Subsequent steps can be generated as follows. For $d = 2^5 = 32$, the operator $U^{(5)}$ is given by

$$U^{(5)} = (U_{\searchrow}U_{\diagup})U_o\big(\zeta_x^{(4)}\big)U^{(4)}. \tag{D6}$$

For $d = 2^6 = 64$, the operator $U^{(6)}$ is given by

$$U^{(6)} = (U_{\nearrow}U_{\nwarrow})U_e\big(\zeta_x^{(5)}\big)U^{(5)}. \tag{D7}$$

We report the spatial distribution of the basis vectors for $n = 5$ and 6 in Figs. 12(d) and 12(e). In general, the operator $U^{(n)}$ can be derived from the operator $U^{(n-1)}$ by applying splitting operators $U_e(U_o)$ for n even (odd) values of n. The application of $U_e U^{(n-1)}(U_o U^{(n-1)})$ on the initial state generates a superposition of two different states with orthogonal coins $|\uparrow\rangle$ and $|\downarrow\rangle$ respectively. They have equal spatial distributions that overlap on some sites. An example is provided in Fig. 13 for the particular case of $n = 5$. In order to remove the overlap between these two states, we apply $U_{\nearrow}U_{\nwarrow}(U_{\searchrow}U_{\diagup})$ operators that translate both orthogonal states until the state is no longer in a superposition.

From these considerations, we write the operator $U^{(n)}$ for $n > 2$ as follows: (1) n odd

$$U^{(n)} = (U_{\searchrow}U_{\diagup})^{f(n)}U_o\big(\zeta_x^{(n-1)}\big)U^{(n-1)} \tag{D8}$$

with $f(n) = 2^{\frac{n-3}{2}} - 1$ and (2) n even

$$U^{(n)} = (U_{\nearrow}U_{\nwarrow})^{g(n)}U_e\big(\zeta_x^{(n-1)}\big)U^{(n-1)} \tag{D9}$$

TABLE VI. Sixteen different basis vectors are obtained when each of the parameters ζ listed takes values $-\pi/2$ or $\pi/2$.

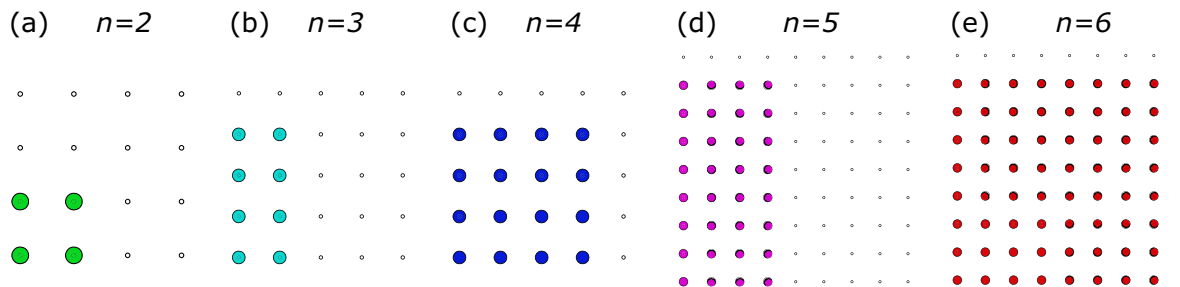| $|\psi_i^{(4)}\rangle$	$\zeta_x^{(1)}$	$\zeta_x^{(2)}$	$\zeta_x^{(3)}$	ζ_y
$|\psi_1^{(4)}\rangle$	$-\frac{\pi}{2}$	$-\frac{\pi}{2}$	$-\frac{\pi}{2}$	$-\frac{\pi}{2}$
$|\psi_2^{(4)}\rangle$	$-\frac{\pi}{2}$	$-\frac{\pi}{2}$	$-\frac{\pi}{2}$	$\frac{\pi}{2}$
$\vdots$	$\vdots$	$\vdots$	$\vdots$	$\vdots$
$|\psi_{15}^{(4)}\rangle$	$\frac{\pi}{2}$	$\frac{\pi}{2}$	$\frac{\pi}{2}$	$-\frac{\pi}{2}$
$|\psi_{16}^{(4)}\rangle$	$\frac{\pi}{2}$	$\frac{\pi}{2}$	$\frac{\pi}{2}$	$\frac{\pi}{2}$

FIG. 12. Spatial distributions of the $|\psi_i^{(n)}\rangle$ basis. We sketch the spatial distributions on the lattice sites of the $|\psi_i^{(n)}\rangle$ basis with dimension $d = 2^n$ with $n = 2, 3, 4, 5, 6$ (a)–(e). The probability at each site is the same and equal to $1/d$.

with $g(n) = 2^{\frac{n}{2}-2} - 1$. We always have n independent parameters $\zeta_x^{(1)}, \zeta_x^{(2)}, \ldots, \zeta_x^{(n-1)}, \zeta_y$ that allows us to generate 2^n basis vectors when they take the values $-\pi/2$ and $\pi/2$ according to Table VII.

Note that the number of steps required in a 2DssQW for generating the basis vectors $|\psi_i^{(n)}\rangle$ scales with $\sqrt{d}$, where $d = 2^n$. Hence, there is a quadratic gain with respect to the 1DQW, where the number of steps scales linearly with d.

The procedure shown above is not the only one that permits generating bases that are mutually unbiased with respect to the computational one. As an example, a basis state for $d = 4$ can be generated as reported in Eq. (30) with a different procedure. More specifically, the basis vector is obtained by applying the operator $U_{\boxtimes}(\zeta_x, \zeta_y)$ to the localized initial state $|0, 0\rangle|+\rangle$. The four different vectors of the basis are generated by setting ζ_x equal to zero, by setting ζ_y equal to $-\pi/2$ and $\pi/2$, and by projecting the final state on the coin state $|+\rangle$ and $|-\rangle$.

APPENDIX E: EXPERIMENTAL DETAILS

1. List of states

We exploit a photonic platform to generate the quantum states by exploiting one, two, and three steps of the quantum walk evolution. Here we provide the list of states that are realized with one and three steps of 2DssQW evolutions.

For target states $|\phi_{\text{tar}}\rangle$, we use the notation in Eqs. (25) and (26). The list of the target states that we have experimentally implemented is reported in the following: (1) one-step states ($N = 1$)

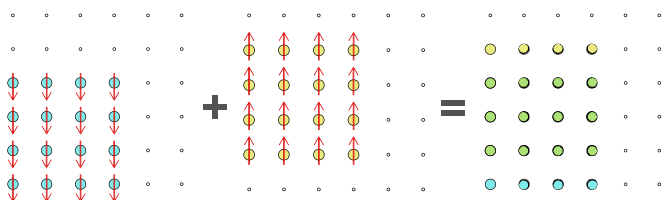$$|\phi\rangle^{(1)} = \frac{1}{\sqrt{2}}\begin{pmatrix} 1 & 0 \\ 0 & 1 \end{pmatrix}$$

FIG. 13. Application of the operator $U_o U^{(n-1)}$ to the initial state $|\psi_0\rangle$ for $n = 5$. We sketch the spatial distributions of the state $U_o U^{(4)}|\psi_0\rangle$. This state is a superposition of two states with orthogonal coins $|\uparrow\rangle$ (yellow) and $|\downarrow\rangle$ (cyan). The probability at each site of the two states is equal to $1/d$ with $d = 2^5$. The spatial distributions of both states overlap (green).

and (2) three-step states ($N = 3$)

$$|\phi_1\rangle^{(3)} \propto \begin{pmatrix} 1 & -(1+2i) & (2+i) & -i \\ -(1+2i) & -3 & 3i & (2+i) \\ (2+i) & 3i & -3 & -(1+2i) \\ -i & (2+i) & -(1+2i) & 1 \end{pmatrix},$$

$$|\phi_2\rangle^{(3)} \propto \begin{pmatrix} 1 & -(1+i) & i & 0 \\ -2 & -(2+i) & -(1-i) & 1 \\ 1 & -(1-i) & -(2+i) & -2 \\ 0 & i & -(1+i) & 1 \end{pmatrix},$$

$$|\phi_3\rangle^{(3)} \propto \begin{pmatrix} 0 & i & 1 & 0 \\ i & 0 & 0 & 1 \\ 1 & 0 & 0 & i \\ 0 & 1 & i & 0 \end{pmatrix}.$$

2. Estimation of the phases by the phase difference values

We have shown the procedure to measure the phase differences $\Delta\delta_{i,j}^{(x)}$ and $\Delta\delta_{i,j}^{(y)}$ between the modes in the output states. Here, we explain how we exploit them to obtain the value of the phase $\delta_{i,j}$. In order to obtain the phase value $\delta_{i,j}$, we define the quantity ε given by $\varepsilon = \varepsilon_x + \varepsilon_y$, where

$$\varepsilon_x = \sum_{i=0}^{N-1}\sum_{j=0}^{N} \frac{\left|\delta_{i,j} - \delta_{i+1,j} - \Delta\delta_{i,j}^{(x)}\right|^2}{\sigma_{i,j}^{(x)2}},$$

$$\varepsilon_y = \sum_{i=0}^{N}\sum_{j=0}^{N-1} \frac{\left|\delta_{i,j} - \delta_{i,j+1} - \Delta\delta_{i,j}^{(y)}\right|^2}{\sigma_{i,j}^{(y)2}}. \qquad \text{(E1)}$$

TABLE VII. Generalization of the basis vectors is obtained when each of the parameters ζ listed takes values $-\pi/2$ or $\pi/2$.

$|\psi_i^{(n)}\rangle$	$\zeta_x^{(1)}$	$\cdots$	$\zeta_x^{(n-1)}$	ζ_y
$|\psi_1^{(n)}\rangle$	$-\frac{\pi}{2}$	$\cdots$	$-\frac{\pi}{2}$	$-\frac{\pi}{2}$
$|\psi_2^{(n)}\rangle$	$-\frac{\pi}{2}$	$\cdots$	$-\frac{\pi}{2}$	$\frac{\pi}{2}$
$\vdots$	$\vdots$	$\vdots$	$\vdots$	$\vdots$
$|\psi_{2^n-1}^{(n)}\rangle$	$\frac{\pi}{2}$	$\cdots$	$\frac{\pi}{2}$	$-\frac{\pi}{2}$
$|\psi_{2^n}^{(n)}\rangle$	$\frac{\pi}{2}$	$\cdots$	$\frac{\pi}{2}$	$\frac{\pi}{2}$

Values $\Delta\delta_{i,j}^{(x)}$ and $\Delta\delta_{i,j}^{(y)}$ are the measured value of the phase differences along x and y direction, the values $\sigma_{i,j}^{(x)}$ and $\sigma_{i,j}^{(y)}$ are the corresponding errors, and the $\delta_{i,j}$ are the independent variables. We minimize the function ε with respect to the independent variables $\delta_{i,j}$ with circular errors. The function ε presents a large number of local minima. In order to improve the capability of the minimization procedure to find the global minimum, we search for all the possible solutions of the following linear system:

$$\begin{aligned}
\delta_{i,j} - \delta_{i+1,j} &= \Delta\delta_{i,j}^{(x)} \\
\delta_{j,i} - \delta_{j,i+1} &= \Delta\delta_{j,i}^{(y)}
\end{aligned} \tag{E2}$$

with $i = 0, \ldots, N$ and $j = 0, \ldots, N-1$. The number of the variables is $(N+1)^2$, while the number of the equations is $2N(N+1)$. This system is overdetermined. Furthermore, it does not consider the error on the $\Delta\delta_{i,j}^{(x)}$ and $\Delta\delta_{i,j}^{(y)}$ values. In order to find a solution for the system, we can delete $N^2 - 1$ equations to obtain a linear system having a single solution. By changing the deleted equations, the obtained solution also changes. Hence, we obtain the complete set of all possible solutions for the system by deleting all the possible subsets of $N^2 - 1$ equations. Then, this set of solutions is used as the initial condition for the effective minimization of function ε. Indeed, the minimization routine explores all the initial points, and it chooses the one for which the cost function takes the minimum value. In this way, we calculated the phase distribution for the states generated with coherent light and single photons. The uncertainties of the phases are obtained through a bootstrapping approach.

[1] R. Kaltenbaek, J. Lavoie, B. Zeng, S. D. Bartlett, and K. J. Resch, Optical one-way quantum computing with a simulated valence-bond solid, Nat. Phys. **6**, 850 (2010).

[2] A. Bocharov, M. Roetteler, and K. M. Svore, Factoring with qutrits: Shor's algorithm on ternary and metaplectic quantum architectures, Phys. Rev. A **96**, 012306 (2017).

[3] X. Wu, S. L. Tomarken, N. A. Petersson, L. A. Martinez, Y. J. Rosen, and J. L. DuBois, High-fidelity software-defined quantum logic on a superconducting qudit, Phys. Rev. Lett. **125**, 170502 (2020).

[4] V. Giovannetti, S. Lloyd, and L. Maccone, Advances in quantum metrology, Nat. Photon. **5**, 222 (2011).

[5] F. Bouchard, R. Fickler, R. W. Boyd, and E. Karimi, High-dimensional quantum cloning and applications to quantum hacking, Sci. Adv. **3**, e1601915 (2017).

[6] M. H. Michael, M. Silveri, R. T. Brierley, V. V. Albert, J. Salmilehto, L. Jiang, and S. M. Girvin, New class of quantum error-correcting codes for a bosonic mode, Phys. Rev. X **6**, 031006 (2016).

[7] P. J. Nadkarni and S. S. Garani, Quantum error correction architecture for qudit stabilizer codes, Phys. Rev. A **103**, 042420 (2021).

[8] H. Bechmann-Pasquinucci and A. Peres, Quantum cryptography with 3-state systems, Phys. Rev. Lett. **85**, 3313 (2000).

[9] N. J. Cerf, M. Bourennane, A. Karlsson, and N. Gisin, Security of quantum key distribution using d-level systems, Phys. Rev. Lett. **88**, 127902 (2002).

[10] N. T. Islam, C. C. W. Lim, C. Cahall, J. Kim, and D. J. Gauthier, Provably secure and high-rate quantum key distribution with time-bin qudits, Sci. Adv. **3**, e1701491 (2017).

[11] O. Morin, K. Huang, J. Liu, H. Le Jeannic, C. Fabre, and J. Laurat, Remote creation of hybrid entanglement between particle-like and wave-like optical qubits, Nat. Photon. **8**, 570 (2014).

[12] H. Jeong, A. Zavatta, M. Kang, S.-W. Lee, L. S. Costanzo, S. Grandi, T. C. Ralph, and M. Bellini, Generation of hybrid entanglement of light, Nat. Photon. **8**, 564 (2014).

[13] K. Huang, H. Le Jeannic, O. Morin, T. Darras, G. Guccione, A. Cavaillès, and J. Laurat, Engineering optical hybrid entanglement between discrete- and continuous-variable states, New J. Phys. **21**, 083033 (2019).

[14] M. Neeley, M. Ansmann, R. C. Bialczak, M. Hofheinz, E. Lucero, A. D. O'Connell, D. Sank, H. Wang, J. Wenner, A. N. Cleland *et al.*, Emulation of a quantum spin with a superconducting phase qudit, Science **325**, 722 (2009).

[15] Y. Zhou, X. Jia, F. Li, C. Xie, and K. Peng, Experimental generation of 8.4 dB entangled state with an optical cavity involving a wedged type-II nonlinear crystal, Opt. Express **23**, 4952 (2015).

[16] M. Müller, S. Diehl, G. Pupillo, and P. Zoller, Engineered open systems and quantum simulations with atoms and ions, Adv. At. Mol. Opt. **61**, 1 (2012).

[17] Y. Ban, X. Chen, J. G. Muga, and E. Y. Sherman, Quantum state engineering of spin-orbit-coupled ultracold atoms in a morse potential, Phys. Rev. A **91**, 023604 (2015).

[18] M. A. Alsahhaf, S. A. Aldaghfag, and S. Abdel-Khalek, Physical properties, field purity, and quantum phase for a two-level atom in photon-added coherent states for the morse potential, J. Russ. Laser Res. **38**, 437 (2017).

[19] E. Bimbard, N. Jain, A. MacRae, and A. Lvovsky, Quantum-optical state engineering up to the two-photon level, Nat. Photon. **4**, 243 (2010).

[20] T. Giordani, E. Polino, S. Emiliani, A. Suprano, L. Innocenti, H. Majury, L. Marrucci, M. Paternostro, A. Ferraro, N. Spagnolo, and F. Sciarrino, Experimental engineering of arbitrary qudit states with discrete-time quantum walks, Phys. Rev. Lett. **122**, 020503 (2019).

[21] P. A. Ameen Yasir and C. M. Chandrashekar, Generation of hyperentangled states and two-dimensional quantum walks using J or q plates and polarization beam splitters, Phys. Rev. A **105**, 012417 (2022).

[22] N. A. Peters, J. T. Barreiro, M. E. Goggin, T.-C. Wei, and P. G. Kwiat, Remote state preparation: Arbitrary remote control of photon polarization, Phys. Rev. Lett. **94**, 150502 (2005).

[23] W.-T. Liu, W. Wu, B.-Q. Ou, P.-X. Chen, C.-Z. Li, and J.-M. Yuan, Experimental remote preparation of arbitrary photon polarization states, Phys. Rev. A **76**, 022308 (2007).

[24] J. Wang, S. Paesani, Y. Ding, R. Santagati, P. Skrzypczyk, A. Salavrakos, J. Tura, R. Augusiak, L. Mančinska, D. Bacco, D. Bonneau, J. W. Silverstone, Q. Gong, A. Acín, K. Rottwitt, L. K. Oxenløwe, J. L. O'Brien, A. Laing, and M. G. Thompson, Multidimensional quantum entanglement with large-scale integrated optics, Science **360**, 285 (2018).

[25] V. Ansari, E. Roccia, M. Santandrea, M. Doostdar, C. Eigner, L. Padberg, I. Gianani, M. Sbroscia, J. M. Donohue, L. Mancino *et al.*, Heralded generation of high-purity ultrashort single photons in programmable temporal shapes, Opt. Express **26**, 2764 (2018).

[26] D. V. Reddy and M. G. Raymer, Engineering temporal-mode-selective frequency conversion in nonlinear optical waveguides: From theory to experiment, Opt. Express **25**, 12952 (2017).

[27] D. V. Reddy and M. G. Raymer, High-selectivity quantum pulse gating of photonic temporal modes using all-optical ramsey interferometry, Optica **5**, 423 (2018).

[28] S. E. Venegas-Andraca, Quantum walks: A comprehensive review, Quant. Info. Proc. **11**, 1015 (2012).

[29] A. Ambainis, Quantum walks and their algorithmic applications, Int. J. Quantum Inform. **01**, 507 (2003).

[30] A. M. Childs, Universal computation by quantum walk, Phys. Rev. Lett. **102**, 180501 (2009).

[31] A. M. Childs, D. Gosset, and Z. Webb, Universal computation by multiparticle quantum walk, Science **339**, 791 (2013).

[32] Z. Yan, Y.-R. Zhang, M. Gong, Y. Wu, Y. Zheng, S. Li, C. Wang, F. Liang, J. Lin, Y. Xu *et al.*, Strongly correlated quantum walks with a 12-qubit superconducting processor, Science **364**, 753 (2019).

[33] M. Gong, S. Wang, C. Zha, M.-C. Chen, H.-L. Huang, Y. Wu, Q. Zhu, Y. Zhao, S. Li, S. Guo *et al.*, Quantum walks on a programmable two-dimensional 62-qubit superconducting processor, Science **372**, 948 (2021).

[34] T. Kitagawa, Topological phenomena in quantum walks: Elementary introduction to the physics of topological phases, Quant. Info. Proc. **11**, 1107 (2012).

[35] T. Kitagawa, M. A. Broome, A. Fedrizzi, M. S. Rudner, E. Berg, I. Kassal, A. Aspuru-Guzik, E. Demler, and A. G. White, Observation of topologically protected bound states in photonic quantum walks, Nat. Commun. **3**, 882 (2012).

[36] F. Cardano, A. D'Errico, A. Dauphin, M. Maffei, B. Piccirillo, C. de Lisio, G. De Filippis, V. Cataudella, E. Santamato, L. Marrucci *et al.*, Detection of zak phases and topological invariants in a chiral quantum walk of twisted photons, Nat. Commun. **8**, 15516 (2017).

[37] S. Barkhofen, T. Nitsche, F. Elster, L. Lorz, A. Gábris, I. Jex, and C. Silberhorn, Measuring topological invariants in disordered discrete-time quantum walks, Phys. Rev. A **96**, 033846 (2017).

[38] C. Chen, X. Ding, J. Qin, Y. He, Y.-H. Luo, M.-C. Chen, C. Liu, X.-L. Wang, W.-J. Zhang, H. Li *et al.*, Observation of topologically protected edge states in a photonic two-dimensional quantum walk, Phys. Rev. Lett. **121**, 100502 (2018).

[39] X. Xu, Q. Wang, M. Heyl, J. C. Budich, W.-W. Pan, Z. Chen, M. Jan, K. Sun, J.-S. Xu, Y.-J. Han, C.-F. Li, and G.-C. Guo, Measuring a dynamical topological order parameter in quantum walks, Light Sci. Appl. **9**, 7 (2020).

[40] M. Ehrhardt, R. Keil, L. J. Maczewsky, C. Dittel, M. Heinrich, and A. Szameit, Exploring complex graphs using three-dimensional quantum walks of correlated photons, Sci. Adv. **7**, eabc5266 (2021).

[41] A. D'Errico, F. Cardano, M. Maffei, A. Dauphin, R. Barboza, C. Esposito, B. Piccirillo, M. Lewenstein, P. Massignan, and L. Marrucci, Two-dimensional topological quantum walks in the momentum space of structured light, Optica **7**, 108 (2020).

[42] V. D'Ambrosio, G. Carvacho, F. Graffitti, C. Vitelli, B. Piccirillo, L. Marrucci, and F. Sciarrino, Entangled vector vortex beams, Phys. Rev. A **94**, 030304(R) (2016).

[43] W. W. Zhang, S. K. Goyal, F. Gao, B. C. Sanders, and C. Simon, Creating cat states in one-dimensional quantum walks using delocalized initial states, New J. Phys. **18**, 093025 (2016).

[44] Y. Zhang, F. S. Roux, T. Konrad, M. Agnew, J. Leach, and A. Forbes, Engineering two-photon high-dimensional states through quantum interference, Sci. Adv. **2**, e1501165 (2016).

[45] S. Moulieras, M. Lewenstein, and G. Puentes, Entanglement engineering and topological protection by discrete-time quantum walks, J. Phys. B **46**, 104005 (2013).

[46] Z. Li, H. Zhang, and H. Zhu, Implementation of generalized measurements on a qudit via quantum walks, Phys. Rev. A **99**, 062342 (2019).

[47] A. Gratsea, M. Lewenstein, and A. Dauphin, Generation of hybrid maximally entangled states in a one-dimensional quantum walk, Quantum Sci. Technol. **5**, 025002 (2020).

[48] A. Gratsea, F. Metz, and T. Busch, Universal and optimal coin sequences for high entanglement generation in 1D discrete time quantum walks, J. Phys. A **53**, 445306 (2020).

[49] T. Giordani, L. Innocenti, A. Suprano, E. Polino, M. Paternostro, N. Spagnolo, F. Sciarrino, and A. Ferraro, Entanglement transfer, accumulation and retrieval via quantum-walk-based qubit-qudit dynamics, New J. Phys. **23**, 023012 (2021).

[50] M. A. Can, A. Klyachko, and A. Shumovsky, Single-particle entanglement, J. Opt. B **7**, L1 (2005).

[51] E. Nagali and F. Sciarrino, Generation of hybrid polarization-orbital angular momentum entangled states, Opt. Express **18**, 18243 (2010).

[52] A. Aiello, F. Töppel, C. Marquardt, E. Giacobino, and G. Leuchs, Quantum- like nonseparable structures in optical beams, New J. Phys. **17**, 043024 (2015).

[53] A. Forbes and I. Nape, Quantum mechanics with patterns of light: Progress in high dimensional and multidimensional entanglement with structured light, AVS Quantum Sci. **1**, 011701 (2019).

[54] E. Karimi, J. Leach, S. Slussarenko, B. Piccirillo, L. Marrucci, L. Chen, W. She, S. Franke-Arnold, M. J. Padgett, and E. Santamato, Spin-orbit hybrid entanglement of photons and quantum contextuality, Phys. Rev. A **82**, 022115 (2010).

[55] Y. Sun, Q.-Y. Wen, and Z. Yuan, High-efficient quantum key distribution based on hybrid entanglement, Opt. Commun. **284**, 527 (2011).

[56] J. Heo, C. H. Hong, J. I. Lim, and H. J. Yang, A quantum communication protocol transferring unknown photons using path-polarization hybrid entanglement, Chin. Phys. Lett. **30**, 040301 (2013).

[57] W. Hao, T. Zhang, X. Chen, and X. Zhou, A hybrid neqr image encryption cryptosystem using two-dimensional quantum walks and quantum coding, Signal Process. **205**, 108890 (2023).

[58] C. Chen, X. Ding, J. Qin, J. Wu, Y. He, C.-Y. Lu, L. Li, X.-J. Liu, B. C. Sanders, and J.-W. Pan, Topological spin texture of chiral edge states in photonic two-dimensional quantum walks, Phys. Rev. Lett. **129**, 046401 (2022).

[59] M. Yamagishi, N. Hatano, K.-I. Imura, and H. Obuse, Proposal of multidimensional quantum walks to explore dirac and schrödinger systems, Phys. Rev. A **107**, 042206 (2023).

[60] L. Innocenti, H. Majury, T. Giordani, N. Spagnolo, F. Sciarrino, M. Paternostro, and A. Ferraro, Quantum state engineering using one-dimensional discrete-time quantum walks, Phys. Rev. A **96**, 062326 (2017).

[61] A. D'Errico, F. Di Colandrea, R. Barboza, A. Dauphin, M. Lewenstein, P. Massignan, L. Marrucci, and F. Cardano, Bulk detection of time-dependent topological transitions in quenched chiral models, Phys. Rev. Res. **2**, 023119 (2020).

[62] C. Esposito, M. R. Barros, A. Durán Hernández, G. Carvacho, F. Di Colandrea, R. Barboza, F. Cardano, N. Spagnolo, L. Marrucci, and F. Sciarrino, Quantum walks of two correlated photons in a 2D synthetic lattice, npj Quantum Inf. **8**, 34 (2022).

[63] A. D'Errico, R. Barboza, R. Tudor, A. Dauphin, P. Massignan, L. Marrucci, and F. Cardano, Bloch–landau–zener dynamics induced by a synthetic field in a photonic quantum walk, APL Photon. **6**, 020802 (2021).

[64] F. Di Colandrea, A. Babazadeh, A. Dauphin, P. Massignan, L. Marrucci, and F. Cardano, Ultra-long quantum walks via spin-orbit photonics, Optica **10**, 324 (2023).

[65] Y. Wang, Z. Hu, B. C. Sanders, and S. Kais, Qudits and high-dimensional quantum computing, Front. Phys. **8**, 589504 (2020).

[66] C.-Q. Ye and T.-Y. Ye, Multi-party quantum private comparison of size relation with d-level single-particle states, Quant. Info. Proc. **17**, 1 (2018).

[67] H.-H. Li, L.-H. Gong, and N.-R. Zhou, New semi-quantum key agreement protocol based on high-dimensional single-particle states, Chin. Phys. B **29**, 110304 (2020).

[68] Y.-R. Li, D.-H. Jiang, Y.-H. Zhang, and X.-Q. Liang, A quantum voting protocol using single-particle states, Quant. Info. Proc. **20**, 1 (2021).

[69] X.-L. Wang, X.-D. Cai, Z.-E. Su, M.-C. Chen, D. Wu, L. Li, N.-L. Liu, C.-Y. Lu, and J.-W. Pan, Quantum teleportation of multiple degrees of freedom of a single photon, Nature (London) **518**, 516 (2015).

[70] X.-Y. Lü, G.-L. Zhu, L.-L. Zheng, and Y. Wu, Entanglement and quantum superposition induced by a single photon, Phys. Rev. A **97**, 033807 (2018).

[71] Y. Li, M. Gessner, W. Li, and A. Smerzi, Hyper- and hybrid nonlocality, Phys. Rev. Lett. **120**, 050404 (2018).

[72] S. Das, G. Paul, and A. Banerji, Hyper-hybrid entanglement, indistinguishability, and two-particle entanglement swapping, Phys. Rev. A **102**, 052401 (2020).

[73] G. Guccione, T. Darras, H. Le Jeannic, V. B. Verma, S. W. Nam, A. Cavaillès, and J. Laurat, Connecting heterogeneous quantum networks by hybrid entanglement swapping, Sci. Adv. **6**, eaba4508 (2020).